Author Manuscript
Accepted for publication in a peer-reviewed journal

NIST National Institute of Standards and Technology • U.S. Department of Commerce

Published in final edited form as:
Mater Struct. 2017 February ; 50: . doi:10.1617/s11527-016-0964-8.

Numerical Simulation of the Freeze-Thaw Behavior of Mortar Containing Deicing Salt Solution

Hadi S. Esmaeeli[1], **Yaghoob Farnam**[1], **Dale P. Bentz**[2], **Pablo D. Zavattieri**[1], and **Jason Weiss**[3,*]

[1]Lyles School of Civil Engineering, Purdue University, 550 Stadium Mall Dr., West Lafayette, IN 47907, USA

[2]Materials and Structural Systems Division, National Institute of Standards and Technology, 100 Bureau Dr., Stop 8615, Gaithersburg, MD 20899, USA

[3]School of Civil & Construction Engineering, Oregon State University, 111 Kearney Hall, Corvallis, OR 97331, USA

Abstract

This paper presents a one-dimensional finite difference model that is developed to describe the freeze-thaw behavior of an air-entrained mortar containing deicing salt solution. A phenomenological model is used to predict the temperature and the heat flow for mortar specimens during cooling and heating. Phase transformations associated with the freezing/melting of water/ice or transition of the eutectic solution from liquid to solid are included in this phenomenological model. The lever rule is used to calculate the quantity of solution that undergoes the phase transformation, thereby simulating the energy released/absorbed during phase transformation. Undercooling and pore size effects are considered in the numerical model. To investigate the effect of pore size distribution, this distribution is considered using the Gibbs-Thomson equation in a saturated mortar specimen. For an air-entrained mortar, the impact of considering pore size (and curvature) on freezing was relatively insignificant; however the impact of pore size is much more significant during melting. The fluid inside pores smaller than 5 nm (i.e., gel pores) has a relatively small contribution in the macroscopic freeze-thaw behavior of mortar specimens within the temperature range used in this study (i.e., +24 °C to −35 °C), and can therefore be neglected for the macroscopic freeze-thaw simulations. A heat sink term is utilized to simulate the heat dissipation during phase transformations. Data from experiments performed using a low-temperature longitudinal guarded comparative calorimeter (LGCC) on mortar specimens fully saturated with various concentration NaCl solutions or partially saturated with water is compared to the numerical results and a promising agreement is generally obtained.

Keywords

Degree of saturation; deicing salt; finite difference method; freeze and thaw; cementitious; pore size distribution; undercooling

*Corresponding author: W. Jason Weiss, jason.weiss@oregonstate.edu.

1. Introduction

Deicing salts are applied to the surface of concrete pavements to melt ice and snow in an effort to improve safety conditions for the traveling public. The solution that is produced (e.g., water-NaCl, $CaCl_2$, $MgCl_2$) can be absorbed into concrete pores. This solution alters the degree of saturation (i.e., the volume ratio of fluid in the specimen as compared to the total maximum volume of fluid that the specimen can hold) of the concrete pavement, the freezing temperature of the solution within the concrete pores, and the damage that may result [1–13].

Prediction of phase transformation within the pores requires an understanding of heat flow within a mortar during a freezing/thawing cycle [14, 15]. For the purpose of this discussion, the term “latent heat” is used to denote the amount of energy released or absorbed during a phase transformation (formation or melting of ice or eutectic solid). The latent heat produced by the phase transformation of the pore solution can be used to quantify the amount of pore solution in concrete that freezes [2]. There are two main phenomena that affect the freezing of pore solution in a mortar/concrete: (1) its pore size distribution and (2) undercooling, as described below.

First, the pore size distribution in concrete influences its freezing. Concrete pores are typically categorized into three main classes: 1) gel pores with a radius smaller than 5 nm that are associated with the formation of cement (binder) hydration products, 2) capillary pores that are the remnants of the original water-filled space between (cement) particles and commonly range from 5 nm to 5 μm in radius, and 3) pores (voids) associated with entrained or entrapped air that range from 5 μm to 10 mm [16–19]. The size of the pores in the concrete can influence the temperature at which freezing occurs. This is described using the Gibbs-Thomson equation [20]. A large fraction of water associated with pore sizes greater than 5 nm (i.e., capillary pores or pores associated with entrained or entrapped air) is susceptible to freezing at a temperature above −10 °C [9, 21, 22]. According to the Gibbs-Thomson equation, the water absorbed in the gel pores will not begin to freeze until the temperature of the specimen drops to about −13 °C [22–24]. It is also worth mentioning that the solution inside concrete pores (i.e., pore solution) contains different ionic species (such as Na^+, K^+, Ca^{++}, and OH^-) [25] that depress its freezing temperature [7]. The absorption of salt solution into the pores can further depress the freezing temperature of this pore solution, due to the presence of additional ions such as Cl^- [5, 26, 27].

Undercooling also influences freezing in concrete. While it is expected that a solution freezes at its characteristic melting point temperature, T_m, freezing usually occurs at a temperature (i.e., T_f) lower than T_m. This reduction in freezing temperature is known as undercooling [28–30] and is primarily due to the fact that solidification (in most cases) requires the presence or formation of nuclei that can trigger the freezing action. Once the heterogeneous nuclei are present in the liquid phase, ice crystals begin to nucleate/grow and consequently the latent heat of fusion is released into the undercooled liquid, increasing the temperature of the liquid toward T_m. Growth of ice continues until the temperature of the liquid reaches T_m [28]. Afterwards, the temperature of the liquid remains at T_m until the entire liquid solidifies, this is known as thermal arrest [28]. After thermal arrest, the amount

of ice increases gradually as the temperature further decreases. Melting however occurs gradually in the pores as the temperature of each pore reaches its T_m value [9, 24, 31]. The amount of ice transformed to solution increases gradually as each set of larger pores in turn reach the associated T_m (according to the Gibbs-Thomson equation) [24, 32].

These two phenomena (i.e., pore size and undercooling) affect the freezing behavior of pore solution simultaneously in the mortar specimen and it may be essential to consider both in the simulation during freezing. In melting, however, only pore size influences the thawing behavior. Numerically, it is feasible to develop a theoretical model based on the heat transfer formulation to predict and simulate phase transformation and heat transfer in materials [33, 34]. One-dimensional finite difference [34–38], two-dimensional finite difference [34, 36, 38–40], control volume [41–44], and finite element [45–47] based methods all have been used to simulate such heat transfer problems. In this paper, a one-dimensional finite difference model is used. In particular, this numerical method approximates the complex solid-liquid interactions in the porous mortar using a fixed grid method [48, 49]. The computational model is applied to estimate the thermal behavior of mortar containing NaCl solutions or just water under freeze-thaw cycles. The formation of ice is quantified by calculating the volume fraction of ice that is produced and the concentration of the remaining fraction of solution during cooling using the lever rule [50, 51]. As the ice grows, the liquid to solid phase transformation releases latent heat, ΔH_f, that increases the temperature of the material locally and slows down the ice growth. An empirical approach is used to account for the sudden latent heat release produced by undercooling. This model is also used to describe, analyze and interpret the experimental data obtained from low-temperature longitudinal guarded comparative calorimeter (LGCC) tests [9,11].

2. Numerical simulation

The main objective of this study is to predict the thermal response of a mortar (considered at a macroscopic scale) that is experiencing phase transformations during a reduction and subsequent increase in specimen temperature (i.e., a freezing and thawing cycle). The goal of the simulations is to quantify the fraction of pore solution that can freeze in an undercooled mortar specimen. The temperature of the specimen can be tracked by solving the heat (energy balance) equation and considering the frozen fraction of the pore solution. The governing equation for the heat transfer within a mortar specimen can be described using the energy balance Equation 1 [54].

$$\frac{\partial}{\partial x}\left[k_m(T)\cdot\frac{\partial T(x,t)}{\partial x}\right]+q_{\text{gen}}-q_{\text{loss}}=\rho_m(T)\cdot C_m^p(T)\cdot\frac{\partial T(x,t)}{\partial t} \quad (1)$$

where $T(x, t)$ is the temperature at location $x(mm)$ and time t(sec), $k_m(T)$ is the thermal conductivity of the mortar specimen [$W/(m\cdot K)$] at temperature T, $\rho_m(T)$ is the density of the mortar specimen (kg/m^3) at temperature T, C_m^p is its specific heat capacity [$J/(kg\cdot K)$] at temperature T, q_{gen} is the rate of generated or consumed heat from any phase change of the pore solution [$J/(m^3\cdot \text{sec})$], and q_{loss} is the rate of heat dissipation (to the environment) in the experiment [$J/(m^3\cdot \text{sec})$].

In Equation 2a, the incorporation of a released/absorbed latent heat term, q_{gen} associated with freezing/melting of the pore solution within a mortar specimen is described. A heat sink term, q_{loss} is also included as shown in Equation 2b to calculate the rate of heat dissipation to the environment (even though insulation is present). This heat term is considered as a fraction of the rate of generated latent heat to simulate the significant heat exchange between the mortar specimen and its surroundings in the lateral directions.

$$q_{\text{gen}}=\Delta H_f \cdot \rho_{\text{so ln}} \cdot v_P \cdot \frac{\partial [v_F(T) \cdot \xi(T)]}{\partial t} \quad 2a$$

$$q_{\text{loss}}=\Delta H_f \cdot h_{\text{loss}} \cdot \rho_{\text{so ln}} \cdot v_P \cdot \frac{\partial [v_F(T) \cdot \xi(T)]}{\partial t} \quad 2b$$

$$q_{\text{gen}} - q_{\text{loss}}=\Delta H^m{}_f \cdot \rho_{\text{so ln}} \cdot v_P \cdot \frac{\partial [v_F(T) \cdot \xi(T)]}{\partial t} \quad 2c$$

where ΔH_f is the latent heat of fusion (kJ/kg), $\rho_{so\,\text{ln}}$ is the density of pore solution (kg/m^3), v_p is the total volume fraction of pores within the mortar specimen (0 to 1), $v_F(T)$ is the volume fraction of the pore solution that can freeze at temperature T (0 to 1), $\xi(T)$ is the frozen volume fraction of freezable pore solution with salt at temperature T (0 to 1), h_{loss} is the heat dissipation coefficient (< 1), and $\Delta H_f^m=\Delta H_f \cdot (1 - h_{\text{loss}})$ is the apparent latent heat measured considering heat dissipation during phase transformation in the system (< ΔH_f).

3. Frozen fraction of pore solution without salt, $v_F(T)$

The mortar specimens contain a pore structure with a broad range of sizes. The pore size can alter the freezing temperature of water [5–7, 27]. To determine the pore size distribution in the mortar specimen and thus to calculate $v_F(T)$, a desorption isotherm was obtained for the mortar using a dynamic vapor sorption analyzer (TA Q5000). The vacuum saturation method is used to fully saturate the mortar specimen (i.e., D_S = 100 %). Therefore, all of the pores, including air voids, are filled with water, to investigate the role of curvature of the pores on the thermal behavior of the mortar. For melting, the pore size distribution obtained from an absorption isotherm is used [55]. Figure 1 provides the desorption-absorption isotherm for the mortar specimen and it correlates the degree of saturation (D_s) to the relative humidity (RH), which is the amount of water vapor present in the specimen expressed as a percentage of the amount needed for saturation at the same temperature [10]. A characteristic hysteresis is observed in the absorption/desorption isotherm in Figure 1, at least partially due to the presence of “ink-bottle” pores.

To calculate $v_F(T)$, two approaches were evaluated in this study: (1) a model with explicit consideration of a continuous pore size distribution, and (2) a phenomenological model with

consideration of only a discrete pore size distribution. The first approach considers the effect of all pore sizes on the freezing process and $v_F(T)$ varies continuously as the temperature changes. In the second approach, the effect of a discrete pore size distribution on ice formation inside the mortar specimen is simplified and a phenomenological model is adapted to simulate the freezing process of water inside the mortar specimen (it considers only two classes of pores-large pores that include all pores except gel pores (the capillary and air entrained/entrapped pores) and small pores (known as gel pores)).

In the phenomenological model, $v_F(T)$ is considered to be a constant value based on three main classes of pores: 1) gel pores, 2) capillary pores, and 3) water-filled pores associated with entrained or entrapped air. To investigate the accuracy of these two approaches, the LGCC test conducted by Farnam et al. [9, 11] was simulated using these two models with consideration of continuous and discrete pore sizes, respectively, and also the thermal behavior of the mortar specimens saturated with water was compared with experimental results obtained in a temperature range between 24 °C and −35 °C.

3.1. A model with consideration of a continuous pore size distribution

Equation 3 describes the Gibbs-Thomson equation that relates the freezing temperature of a liquid inside a porous material to the pore radius.

$$\frac{2\gamma_{CL}}{r^*} \approx \left(\frac{S_L - S_C}{V_L}\right)(T_m - T_f)(r^*) \quad 3$$

where γ_{CL} is the crystal/liquid interfacial energy (J/m^2), r^* is the radius of the pore for homogeneous nucleation (m), S_L and S_C are the molar entropies of the liquid and crystalline phases [$J/(mol \cdot K)$], V_L is the molar volume of the liquid (m^3/mol), T_m is the melting temperature (K), and T_f is the freezing temperature as a function of pore radius (K)[24, 56]. Therefore, the temperature at which ice begins to form can be predicted as a function of critical pore radius r^* by solving Equation 3 for T_f[20, 24, 32].

Figure 2 displays the relationship between the size of the pore and the temperature that is needed to freeze water inside the pore, $T_f(r^*)$. At a temperature above $T_f(r^*)$, no phase transformation occurs inside the pores with radius less than r^*. Once the temperature reaches the associated freezing temperature, ice begins to form inside the pores with radii of r^*. Afterwards, ice propagates into the smaller pores, but only as the temperature drops further. This process is reversed during melting.

The Kelvin-Young-Laplace equation can be used to correlate the pore radius to the relative humidity (RH) in a water-filled pore as described in Equation 4 [57, 58].

$$r^* = \left(\frac{2\gamma}{\ln(RH)}\right) \cdot \left(\frac{V_m}{RT}\right) \quad 4$$

In this study, the Kelvin-Young-Laplace equation (Equation 4) was used alongside the Gibbs-Thomson equation (Equation 3) to obtain the relationship between $v_F(T)$ and pore size in the mortar specimen based on its measured desorption isotherm (Figure 1). At a temperature of −35 °C, solution absorbed into the mortar pores with sizes greater than 1.47 nm is susceptible to freezing as shown in Figure 2. Figure 2 also displays the process of ice formation in a porous material, as the ice forms inside the larger pores initially. Ice invades into the smaller pores progressively as the temperature drops. Figure 3 shows that 72 % of the solution absorbed in the pores by volume can freeze between 0 °C and −35 °C. For the case of melting, the formed ice in the pores is similarly considered to melt gradually according to the Gibbs-Thomson equation (Equation 3). In this work, it is assumed that $1 = v_{air} + (D_S / 100)$ and $(D_s / 100) = v_w(r < r^*) + v_F(r > r^*)$ where v_{air} and v_w are the volume fraction of air and non-freezable pore solution in the total pores (0 to 1), respectively. To investigate the role of pore sizes, all of the pores with various sizes are assumed to be filled with water in this section, i.e., $v_{air} = 0$. It should be mentioned that the LGCC test was conducted within a temperature range between 24 °C and −35 °C.

3.2. A phenomenological model with consideration of a discrete pore size distribution

Although the continuous pore size distribution can be estimated to determine the volume fraction of freezable pore solution, this measurement is generally not available for field/commercial concretes. In this paper, a phenomenological model is developed to use in practice, when knowledge of the continuous pore size distribution is not available. Since the freezing and thawing responses of most cementitious systems are dominated by the category of relatively large pores (i.e., capillary, air-entrained, and air-entrapped pores), a discrete pore size of 5 nm (a pre-defined critical pore size as the division between gel and capillary pores) can be utilized as a criterion to differentiate the freezable and non-freezable pore solution [16, 21, 59]. For a mortar sample saturated with deionized water, this critical pore radius corresponds to a relative humidity (RH) equal to 81 %, at which point all of the gel pores are filled by solution [57].

The corresponding freezing temperature of water in pores with a size of 5 nm is about −13 °C according to the Gibbs-Thomson equation as displayed in Figure 2. Figure 3 displays the relation between derived volume fraction of freezable pore solution, v_F from associated relative humidity measured in experiments, and pore radius, r^*, using equation 4. The corresponding volume fraction of freezable pore solution, v_F, in pores with size greater than 5 nm is measured to be 60 % with respect to the total volume fraction of pores displayed in this figure. Consequently, the volume of freezable pore solution in the phenomenological model is underestimated by about 16 % with respect to the model with direct consideration of pore size distribution assuming pure water to be the solution in the pores. This implies that 60 % of the total solution by volume, corresponding to the solution that is absorbed into large pores (i.e., capillary pores, air-entrained pores, and air-entrapped pores) begins to transform to ice instantaneously and the gradual process of ice formation in the remainder of the freezable pores (i.e., smaller pores, containing a lower volume fraction) will be neglected. Therefore, the radius of curvature (pore size) would have a relatively small impact on the macroscopic freezing response of the air-entrained mortar specimen and the

approach of a discrete pore size distribution will be implemented in the numerical model to investigate the thermal behavior of mortar specimens containing NaCl solutions.

4. Frozen fraction of pore solution with salt, $\xi(T)$

For the case where the pores are water-filled (0 % NaCl), the value of $\upsilon_F(T)$ can be used to determine the latent heat released/absorbed when the temperature of the specimen reaches freezing/melting temperatures. In the case where the pores are filled with NaCl solution, the presence of this salt alters the freezing/melting behavior. The phase equilibrium of NaCl solution is shown in Figure 4. In this figure, the liquidus line shows the point at which ice begins to form within the NaCl solution. Above the liquidus line, no ice may be detected (i.e., point 1 in Figure 4). A mixture of ice and salt solution with varying concentration that follows the liquidus line exists between the liquidus and eutectic temperatures (T_{eut}= −21.1 °C), which is commonly known as the freezing region (i.e., point 2). At T_{eut} (i.e., the eutectic line), the formation of ice is complete and all the solution converts to a solid eutectic composition as the temperature of the solution decreases further, which is described in more detail in section 8.2. Below this temperature, it is assumed that no solution exists in the capillary, air-entrained and air-entrapped pores. According to solidification principles [28], the lever rule can be used to determine the amount of ice when the specimen temperature is between the liquidus and eutectic lines.

The frozen fraction of the freezable pore solution $\xi(T)$ was used in the numerical simulation to calculate the amount of latent heat released/absorbed during freezing/melting at each time step for the mortar specimen saturated with NaCl solution. The lever rule, given in Equation 5, was employed in this study as a tool to compute the amount of produced ice within the freezing region for NaCl solutions in a mortar specimen.

$$\xi(T)=\frac{c_s(T)-c_0}{c_s(T)} \quad 5$$

where $c_s(T)$, the concentration of the ice solution mixture, can be estimated as a function of solution temperature by using Equation 6 [11]:

$$c_s(T)=a_2\times T^2(x,t)+a_1\times T(x,t)+a_0 \qquad -35^\circ C\le T(x,t)\le 24^\circ C \quad 6$$

where a_0=0.003385, a_1=−0.016362 [1/(°C)], a_2=−0.000264 [1/(°C^2)], and c_0 is the initial concentration of NaCl solution above the liquidus line by mass (%). The coefficients in Equation 6 fit the $c_s(T)$ curve on data points derived from the phase diagram of aqueous NaCl solutions with R^2=0.999 as the measure of goodness-of-fit.

The frozen fraction of the freezable pore solution $\xi(T)$ was calculated for bulk solutions containing 0 %, 5 %, 10 %, and 23.3 % NaCl (by mass) and is depicted in Figure 4. This figure is divided into three temperature ranges for solution with NaCl concentrations of 0 %, 5 %, 10 %, and 23.3 % : (1) −35 °C $\le T(x,t) \le$ −21.1 °C = T_{eut} where the temperature of

solution is below T_{eut} and the entire solution solidifies; (2) −21.1 °C ≤ $T(x,t)$ ≤0 °C where both liquid and solid phases (i.e., ice and solution) coexist; (3) 0 °C < $T(x,t)$ ≤24 °C where no phase transformation occurs and the solution remains in its liquid state.

Ice formation or solidification of eutectic composition requires removal of sufficient heat/energy to compensate for the latent heat associated with the phase transformation. A considerable amount of latent heat can be released during solidification. Eutectic latent heat for NaCl solution was measured using a low-temperature differential scanning calorimeter and obtained to be ΔH_{eut}= 135 kJ/kg ± 5 kJ/kg. The standard deviation for eutectic latent heat was determined on three mortar specimens containing NaCl solution with 5 %, 10 %, and 23.3 % NaCl concentrations. The latent heat associated with ice formation was also considered to be ΔH_{ice}= 332.4 kJ/kg ± 2 kJ/kg over the range of −35 °C ≤ $T(x,t)$ ≤0 [14, 24, 56]. The heat of fusion $\Delta H_{melting}$ was given with a relative error < 0.25 % by Equation 7 [24]:

$$\Delta H_{\mathrm{melting}}(T)(\mathrm{kJ/kg}) \approx 333.8(\mathrm{kJ/kg}) + 1.79[\mathrm{kJ/(kg \cdot K)}] \cdot (T - T_m) \quad (7)$$

The rate of ice formation within mortar pores was considered in the numerical simulation by evaluating. $\xi(T)$.

5. Effective thermal properties of mortar specimen

To develop a reliable numerical simulation at the macro-scale, it is essential to properly define the material properties. This section discusses how the thermal properties of the mortar specimen as a composite are defined for the proposed finite difference model with the consideration of two approaches concerning the distribution of pore sizes, namely continuous and discrete.

5.1. Thermal Conductivity

The effective medium theory (EMT) [61] can be used to define properties of a composite material for a heterogeneous mixture. For mortar specimens either partially or fully saturated with water or fully saturated with NaCl solution at different concentrations, the thermal conductivity of the mortar (k_m) was estimated using the EMT formulation as described in Equation 8 and shown in Figure 5a:

$$k_m = k_{\mathrm{dry}} \cdot \frac{2(1-\nu_p) \cdot k_{\mathrm{dry}} + (1+2\nu_p) \cdot k_p}{(2+\nu_p) \cdot k_{\mathrm{dry}} + (1-\nu_p) \cdot k_p} \quad (8)$$

where k_{dry} is the thermal conductivity of the dry mortar specimen, k_p is the thermal conductivity of the material in the pores, and v_p is again the total volume fraction of pores.

Depending on the temperature and saturation state, pores in the mortar specimen may contain various constituents including air, ice, or NaCl solutions with different concentrations. The amount of solution and air in the mortar depends on its degree of

saturation (D_S). The temperature of the mortar specimen can also change the amount of solution and ice in mortar pores as described in sections 3 and 4. The change in the amount of air, ice, or solution can substantially alter the thermal conductivity of the mortar specimen due to the considerable differences between the thermal conductivities of air, solid ice, and solution (Table 1).

A parallel model [62] was employed to determine the effective k_P as a function of the volume fractions and thermal conductivities of each component (i.e., k_{air}, k_{ice}, and $k_{so\,ln}$), as described in Equation 9.

$$k_P = k_{\text{air}} \cdot v_{\text{air}} + v_f \cdot [k_{\text{ice}} \cdot \xi + (1-\xi)\, k_{\text{so ln}}] + k_{\text{so ln}} \cdot v_w \quad 9$$

where k_{air} is the thermal conductivity of air, $v_{air} = 1 - (D_S / 100)$ is the volume fraction of air in the mortar pores, k_{ice} is the thermal conductivity of ice, and $k_{so\,ln}$ is the thermal conductivity of the remnant pore solution within the mortar pores. Following the work of Farnam [9], no considerable changes of dimensions of the mortar specimens were observed. Therefore, the volume change is neglected in the thermal modeling of a macro-scale mortar specimen ($v_{air} = 1 - (D_S / 100)$. However, the variation of physical and thermal properties of components of the mortar specimen may lead to a change in the volume of a micro-scale specimen.

It is worth mentioning that the unfrozen solution may exist in (1) smaller pores with an invariable NaCl concentration, and (2) larger pores which contain frozen solution (ice) and a NaCl solution with a higher concentration. The thermal properties of NaCl solution in the smaller pores are provided in Table 1; however, the thermal properties of NaCl solution with variable concentration in the larger pores can be determined knowing the frozen fraction and the Lever rule. The corresponding thermal conductivities of air, ice, NaCl solution with different concentrations, and dry mortar are also provided in Table 1.

5.2 Density, ρ

The law of mixtures (a weighted mean) can be used to predict the density of a composite material. An effective density for mortar specimens (ρ_m) was estimated using the law of mixtures and is described in Equation 10 and shown in Figure 5b.

$$\rho_m = \rho_{\text{dry}} \cdot (1 - \nu_P) + \rho_P \cdot \nu_P \quad 10$$

where ρ_{dry} is the density of the dry mortar and ρ_P is the effective density of the materials in the mortar pores (i.e., air, ice, and solution).

The law of mixtures was again employed to obtain the effective density of the materials in the mortar's pores (i.e., ρ_P) as described in Equation 11.

$$\rho_P = \rho_{\text{air}} \cdot v_{\text{air}} + v_F \cdot [\rho_{\text{ice}} \cdot \xi + (1-\xi)\, \rho_{\text{so ln}}] + \rho_{\text{so ln}} \cdot v_w \quad 11$$

where ρ_{air}, ρ_{ice}, and $\rho_{so\,ln}$ are the densities of air, ice, and solution, respectively. The corresponding densities of air, ice, NaCl solution with different concentrations, and dry mortar are also provided in Table 1.

5.3. Specific heat capacity, C^p

The process of determining an effective specific heat capacity is conceptually similar to determining an effective density [70]. The effective specific heat capacity for a composite mortar specimen C_m^p was calculated using Equation 12 and is shown in Figure 5c.

$$C_m{}^p \cdot \rho_m = C_{\mathrm{dry}}{}^p \cdot \rho_{\mathrm{dry}} \cdot (1-\nu_P) + C_P{}^p \cdot \rho_P \cdot (\nu_P) \quad 12$$

where C_{dry}^p is the specific heat capacity of the dry mortar and C_F^p is the effective specific heat capacity of materials in the mortar pores (i.e., air, ice and solution) which can be calculated using Equation 13.

$$C_P^p \cdot \rho_P = C_{\mathrm{air}}^p \cdot \rho_{\mathrm{air}} \cdot v_{\mathrm{air}} + \{v_P \cdot [C_{\mathrm{ice}}^p \cdot \rho_{\mathrm{ice}} \cdot \xi + C_{\mathrm{so\,ln}}^p \cdot \rho_{\mathrm{so\,ln}} \cdot (1-\xi)] + C_{\mathrm{so\,ln}}^p \cdot \rho_{\mathrm{so\,ln}} \cdot (v_w)\} \quad 13$$

where C_{air}^p, C_{ice}^p, and $C_{\mathrm{so\,ln}}^p$ are the specific heat capacities for air, ice, and solution, respectively. The corresponding specific heat capacities of air, ice, NaCl solution with different concentrations, and dry mortar are provided in Table 1.

6. Configuration of numerical simulation and boundary conditions

Following the work by Farnam et al. [9], the LGCC test was simulated to quantify heat flow and predict the temperature profiles of the mortar specimens. Two types of experimental data are used: 1) fully saturated mortar specimens (i.e., 100 % degree of saturation) with solutions containing 0 %, 5 %, 10 %, and 23.3 % NaCl (by mass), and 2) specimens saturated partially with water (i.e., no NaCl involved in the solution) at degrees of saturation equal to 75 %, 85 %, 95 %, and 100 %. The procedures used for preparation of fully saturated and partially saturated mortar specimens were addressed in previous experimental works [9, 12, 71].

The experimental conditions of one-dimensional heat transfer were provided in the LGCC experiment by using a heat sink at the bottom, longitudinal insulation on the sides, and foam as a thermal insulation around the system to minimize the heat dissipation from the experimental apparatus (Figure 6a). However, a difference between the measured released heat in an LGCC experiment and the associated enthalpy of fusion of phase change materials (i.e., Methyl Laurate and Paraffin Oil), likely due to experimental imperfections (thermal bridges, heat leaks, etc.), was observed. Therefore, h_{loss}, a heat loss coefficient, is employed to simulate the energy dissipation in the experimental system which is estimated as a 40 % to 60 % heat loss [72]. It is worth mentioning that the advection of heat to simulate the water transport occurring during the freeze/thaw cycle is neglected in this numerical investigation.

Two reference (meter) bars made of Pyroceram code 9606† with known thermal properties were used to measure the heat flow passing through the mortar specimen in the experiment (see Figure 6a.

The first step in the numerical approach was to discretize the experimental setup by a finite difference method using an appropriate grid spacing size, Δx of 1 (mm) and time step, Δt of 0.05 (sec). The initial temperature of the entire experimental setup was set equal to the ambient temperature $T(x, t=0) = 24$ (°C) as displayed in Figure 6b. The temperature at the bottom of the LGCC experiment, $T(x = 1\ mm, t)$ (see Figure 6a) varied in the numerical simulation as a function of time according to the LGCC experimental protocol (Figure 6c). A heat convection coefficient $h_{conv} = 100$ W/(m^2·K) is employed to simulate the heat transfer between the air and the foam on the top [54]. Even though the insulating foam has a quite small thermal diffusivity parameter, significant heat energy is still transferred to the environment, resulting in a slight temperature differential between the top of the foam and the ambient environment. The relevant thermal properties of the thermally conductive pad, foam, and Pyroceram code 9606 used in the modeling are listed in Table 2.

Figure 7 displays a flow chart of the one-dimensional explicit finite difference method adopted to simulate the saturated mortar specimen containing de-ionized water and NaCl solution with various concentrations. First, the thermal properties of components of the mortar specimen, temporal and spatial step sizes, and thermal initial and boundary conditions are determined. All of the discretized layers (i.e. x = 1 mm to x = 204 mm) are employed to simulate the heat transfer for the LGCC experiment; however, only the finite layers of the mortar specimen (i.e., x = 32 mm to x = 83 mm) are investigated in this figure. During phase transformation of the pore solution in the mortar specimen filled with de-ionized water, two approaches of consideration of either a discrete pore size distribution or a continuous pore size distribution were employed, as discussed in section 3. The approach of using a distribution of continuous pore sizes introduces a progressive ice formation/melting in the pores that is simulated using equations 3 and 4 and figure 1; however, the volume fraction of pores with the size greater than 5 nm ($v_F = 60$ %) is considered to simulate the instantaneous ice formation/melting occuring in the approach of using discrete pore sizes. Additionally, the progressive fraction of produced/melting ice is calculated using the lever rule as discussed in section 4.

7. Undercooling

The freezing temperature T_f is the point at which solidification of a liquid occurs, whereas a melting temperature T_m is the point at which a solid melts. In most materials, T_f is usually lower than T_m because of undercooling [28–30]. Therefore, no ice may be formed until the temperature reaches T_f (see Figure 4a). The values of T_f and T_m are obtained directly from the LGCC experiment [9] and are reported in Table 3.

†Certain commercial products are identified in this paper to specify the materials used and procedures employed. In no case does such identification imply endorsement or recommendation by the National Institute of Standards and Technology or Purdue University, nor does it indicate that the products are necessarily the best available for the purpose.

The specimen size and cooling rate of the specimen may alter the degree of undercooling [27]. In general, less undercooling is observed for larger specimens (greater chance of a suitable nucleation source being present), while more undercooling is observed when a greater cooling rate is employed. In the LGCC test (a 25 mm × 25 mm × 50 mm mortar specimen size), the freezing was observed at −6.1 °C when the mortar was saturated with water.

When the temperature of the bottom layer reaches T_f, the layers with temperatures lower than T_m are allowed to begin to produce ice instantaneously and thus the associated heat release results in increasing the temperature toward T_m. Subsequently, the temperature of the layer remains unchanged at T_m until the entire liquid within that layer transforms into ice. Since the numerical model with a discrete pore size distribution is considered to investigate the undercooling effect on thermal behavior of the mortar specimen, nearly 60 % of the pores by volume (i.e., nearly all of the capillary pores, air-entrained pores, and air-entrapped pores) nucleate ice instantaneously for the case of the mortar specimen saturated with deionized water (solution with 0 % NaCl concentration), as shown in Figure 8.

Figure 8 illustrates the effect of considering undercooling on the thermal behavior of the simulated mortar specimens saturated with de-ionized water solution compared with the model without undercooling. The heat loss coefficient, h_{loss} is assumed to be a constant value of 60 % in this figure. Similar to the observed experimental thermal behavior of the mortar specimen [9], a temperature rise at the freezing point was observed in the phenomenological numerical model when undercooling was included, whereas no abrupt temperature ascent was observed without including undercooling. It is worth mentioning that no considerable changes in the dimensions of the mortar specimens were measured during the freezing and melting processes in the experiment.

8. Results

8.1. Mortar specimens saturated with water

In this section, mortar specimens saturated with water at 75 %, 85 %, 95 % and 100 % degrees of saturation (D_S) and the effect of pore size distribution are numerically investigated.

8.1.1. Fully saturated mortar specimen—Two numerical models, with either a continuous or discrete pore size distribution, are investigated in this section. Figure 9 shows the experimental and numerical results for the thermal behavior of mortar specimens that were saturated (i.e., D_S = 100 %) with water. The heat loss coefficient, h_{loss} is assumed to be a constant value of 60 % in this figure. The model with a discrete pore size distribution only considers the instantaneous freezing of the pore solution that can freeze (v_F = 60 %), whereas the model with the continuous pore size distribution also considers an additional process of gradual freezing of the pore solution (v_F = 72 %) as displayed in Figure 9c. Figure 9a indicates the numerical and experimental temperature profile for the saturated mortar specimen at the bottom layer in the LGCC experiment setup (i.e., x = 32 mm). A nearly instantaneous temperature rise that occurred at the moment of freezing can be observed, demonstrating the instantaneous freezing due to the temperature of the first finite

difference layer of the mortar specimen (i.e., $x = 32$ mm) reaching the freezing temperature of (undercooled) water in the mortar specimen ($T_f = -6.1$ °C). However, the model with a continuous pore size distribution considers that the remaining amount of unfrozen water in the pores transforms to ice gradually until the temperature reaches −35 °C.

The model with a discrete pore size distribution considers the ice melting to occur by absorbing sufficient heat at the melting temperature of the large frozen pores observed in the experiment ($T_m = 0$ °C). In the model with a continuous pore size distribution included, the ice formed in the pores is considered to melt gradually starting at −35 °C [24], based on the measured absorption isotherm for the mortar.

The heat flow is obtained using the numerical simulation to evaluate the role of pore size distribution and compared to the experimental data shown in Figure 9b. The formation of ice in the pore solution results in an exothermic peak, which is representative of the latent heat release during a freezing cycle. In the model with a discrete pore size distribution, the exothermic peak is considered to occur at T_f and subsequently ceases when the entire amount of latent heat has been emitted to the surroundings. The endothermic peak begins as a gradual process at 0 °C, until all of the previously formed ice melts inside the frozen pores.

Conversely, the exothermic peak is extended to the end of the freezing cycle (−35 °C) due to gradual ice nucleation inside the smaller pores in the model with a continuous pore size distribution. For the case of melting, the endothermic peak is considered to occur gradually as a function of temperature and the pore size.

Therefore, the melting curve extends progressively to 0 °C, owing to the broad range of pore sizes in the model with a continuous pore size distribution. It is concluded that the consideration of pore size distribution can reasonably be neglected during the freezing process due to undercooling, whereas the melting of formed ice indicated a gradual process as the temperature increases in both the experimental data and the model with a continuous pore size distribution.

8.1.2. Partially saturated mortar specimen—The amount of heat released during freezing $\left(\Delta H_m^F\right)$ was obtained using the numerical simulation for mortar specimens saturated at different degrees of saturation with the discrete pore size distribution model and is compared with experimental results in Figure 10. For partially saturated samples, the value of v_F was calculated using $v_F = D_S - v_w$, where v_w is the volume fraction of pores with the size less than 5 nm ($v_w = 40$ %). The results for these partially saturated mortar specimens are the experimental investigation of this work, whereas the experimental data of the fully saturated mortar specimen was already published [9]. Two heat dissipation coefficients of 40 % and 60 % are considered as discussed in section 6. The coefficient of variation for the experimental results is obtained as 8.6 %. The numerical simulation predicts greater heat release than that obtained in the experiment due to further experimental imperfections.

8.2. Mortar specimens saturated with NaCl solution

The role of NaCl concentration in the pore solution on the thermal behavior of the mortar specimens was also investigated. The process of solidification of the brine solution absorbed in the large pores with a high degree of connectivity is investigated in this model. Therefore, the volume fraction of freezable pore solution containing NaCl solution is assumed to be 60 %. Afterwards, the parameter $\xi(T)$ is employed to calculate the volume fraction of frozen pore solution $v_F(T)^*\xi(T)=0.6^*\xi(T)$ using the Lever rule (based on the phase diagram of NaCl solution). Since it is proposed that the pores larger than gel pores are susceptible to freezing in this numerical model, the size of a salt crystal is sufficiently large so as not to increase its solubility correspondingly. As mentioned in section 7, undercooling compels the solutions inside the porous media to freeze at a temperature below their melting points which can result in an instantaneous solidification of a relatively large fraction of pore solution within the mortar specimen (see Table 3). After this sudden freezing, a gradual phase transformation of the water phase of the solution to ice is hypothesized to occur for the remaining solution in the mortar specimen saturated with NaCl solution. This was computed by using the lever rule approach to solidify the remaining unfrozen fraction of solution (excluding the eutectic solution) until the temperature of each layer reaches $T_{eut} = -21.1\ ^{\circ}C$. For the case of mortar specimens saturated with 23.3 % NaCl solution ($c_{eut} = 23.3\%$), no ice is formed until the temperature decreases to T_{eut}.

At this temperature, the unfrozen eutectic solution begins to transform to eutectic ice gradually. Two different procedures are proposed to investigate the role of eutectic solution solidification on the macro-scale thermal response of the mortar specimen. The first method considers that the eutectic solution, the remaining unfrozen solution, can gradually form eutectic ice by releasing the eutectic latent heat as observed in the experiment shown in Figure 11a [9]. The second method was to allow the eutectic solution to migrate to the adjacent accessible pores with smaller sizes to avoid the formation of eutectic ice in the numerical simulation. Finally, the numerical results were compared with macro-scale experimental data. The numerical and experimental results of heat flow of two mortar specimens saturated by NaCl solutions with 5 % and 10 % concentrations are compared in Figure 11a. The variation of the two numerical models is calculated as 3 % which indicates that the eutectic phase transformation of the NaCl solution should be considered in the numerical modeling. Figure 11b shows the heat flow as a function of time obtained from the numerical simulation for the specimen saturated with NaCl solution while this figure compares the thermal behavior of a mortar specimen with and without undercooling. First, a broader exothermic peak in the heat flow is observed for the numerical simulation without undercooling, since a more gradual freezing is considered. Second, the ice formation occurs earlier in the case of the mortar specimen without including undercooling, since the freezing point T_f is assumed to be identical to the melting temperature T_m. Third, the exothermic peak becomes smaller by increasing the NaCl solution concentration, since a lower volume fraction of pore solution freezes at the corresponding freezing point T_f, which results in a lower heat release through the mortar specimen. Fourth, the exothermic peak of the mortar specimens saturated with greater NaCl solution concentrations occurs later due to depression of the freezing point T_f. The heat loss coefficient, h_{loss} is assumed to be a constant value of 60 % in this figure. Figure 12 displays how pore solution solidifies/melts during cooling/

heating at the bottom and top layers (surfaces) of the mortar specimen since the temperature difference is the maximum between these layers. At the bottom layer, solution containing NaCl first freezes suddenly when reaching T_f due to undercooling effects. Afterwards, ice gradually forms as the temperature further decreases until the temperature reaches T_{eut} at the bottom layer of the mortar specimen. At T_{eut}, all liquid solidifies in the capillary, entrained air, and entrapped air pores.

As described in section 7, at the moment of sudden freezing (when the temperature of the bottom layer reaches T_f), the portion of the mortar specimen whose temperature is between T_f and T_m was allowed to freeze instantaneously. Since the temperature of the top layer of the mortar specimen is higher than the temperature at its bottom layer during a cooling cycle, a lesser amount of ice is produced at the top layer during the sudden freezing (i.e., undercooling) in comparison to the bottom layer, as can be seen in Figure 12. The remainder of the pore solution begins to freeze as the temperature of the layer drops. This solidification process is similar between the bottom and top layers of the mortar specimen containing 0 % NaCl solution, since this process takes place immediately (0.04 seconds). During heating, the melting transformation occurs gradually and the amount of ice can be simply calculated based on the lever rule, since no undercooling occurs.

It is worth mentioning that there is therefore relatively no difference in the melting behavior of pore solution between the top and the bottom layers of the mortar specimen. Figure 13 shows the accumulated released/absorbed heat by the mortar specimen as a function of its bottom layer temperature (i.e., (x = 32 mm)). Pore solutions containing 0 %, 5 %, and 10 % NaCl illustrate a relatively extreme heat emission due to freezing, while the solution containing 23.3 % NaCl releases relatively little energy as it is only composed of the eutectic composition (see Figure 13a). A snapback (rise) of temperature is observed at freezing onset due to the undercooling of pore solution. Figure 13b displays how the specimen absorbs heat during heating/melting. Since melting is a gradual process, the heat absorption occurs at a relatively gradual rate with respect to the freezing process. It is worth mentioning that the total amount of released heat during freezing is identical to the total amount of absorbed heat during melting in the system. The heat loss coefficient, h_{loss} is assumed to be a constant value of 60 % in this figure.

The amount of heat released during freezing $\left(\Delta H_m^F\right)$ is numerically obtained and plotted as a function of NaCl concentration and compared with experimental results in Figure 14. It is worth mentioning that the coefficient of variation for the experimental results is obtained as 8.6 %, based on three replicate specimens. The numerical results are calculated by considering the two coefficients of heat dissipation h_{loss} to compare to the experimental data. Considering these heat dissipation coefficients, the coefficient of variation between experimental result and numerical results with 40 % and 60 % are obtained as 36 % and 9 %, respectively. The numerical over-prediction of latent heat emission is caused by further experimental imperfections.

9. Summary and Conclusion

In this paper, a one-dimensional finite difference numerical model was used to predict the macroscopic freeze-thaw behavior of air-entrained mortar specimens. The effective thermal properties of the composite mortar were estimated using homogenization techniques. The role of curvature, owing to a broad range of pore sizes, was considered in calculating the volume fraction of freezable pore solution exposed to freezing/thawing cycles using measured absorption-desorption isotherms. It was concluded that the role of pore size (or curvature) on the macroscopic behavior of the air entrained mortar specimen was negligible during freezing due to the quantity of larger pore sizes in realistic mixtures and undercooling, whereas the role of curvature had a considerable impact on the macroscopic behavior of the frozen mortar specimen during melting. The lever rule approach, derived from a phase diagram of the NaCl-water solution, and undercooling were adopted in the numerical model. It was concluded that this model can simulate the freezing and thawing process of mortar specimens saturated with water or various NaCl solutions to predict the thermal behavior of mortar specimens at various degrees of saturation or saturated with various concentrations of NaCl solutions.

The computational results were compared to the experimental ones obtained for mortar specimens saturated with NaCl solution using a low-temperature longitudinal guarded comparative calorimeter (LGCC). A lower amount of heat release (or freezable fraction of pore solutions) was observed in the experiment than the theoretical value predicted based on the measured desorption isotherm. The difference may be mainly due to experimental conditions allowing significant heat dissipation within the LGCC experiment. To justify the experimental under-estimation of heat release, two heat loss coefficients of 40 % and 60 % were evaluated to validate the numerical results. Accordingly, a better agreement was exhibited between the numerical results and the experimental data.

Acknowledgments

This work was supported by the Federal Aviation Administration (FAA) through PEGASAS center as Heated Airport Pavements Project (Task 1-C) and Joint Transportation Research Program (JTRP) administered by the Indiana Department of Transportation (SPR-3864). The authors would like to acknowledge the support that has made its operation possible. The contents of this paper reflect the views of the authors, who are responsible for the facts and the accuracy of the data presented herein, and do not necessarily reflect the official views or policies of the FAA and JTRP.

References

1. Powers TC, Willis TF. The air requirement of frost resistant concrete. Highw Res Board. 1950; 29:184–211.
2. Powers TC. A working hypothesis for further studies of frost resistance of concrete. Am Concr Cem Portl Cem Assoc. 1945; 41:245–272.
3. Powers TC. The physical structure and engineering properties of concrete. 1900
4. Litvan G. Frost action in cement in the presence of De-Icers. Cem Concr Res. 1976; 6:351–356.
5. Scherer G. Crystallization in pores. Cem Concr Res. 1999; 29:1347–1358.
6. Kaufmann J. Experimental identification of damage mechanisms in cementitious porous materials on phase transition of pore solution under deicing salt attack. École polytechnique fédérale de Lausanne (EPFL). 2000

7. Mehta, PK.; Monteiro, PJ. Concrete: Microstructure, Properties, and Materials. New York: McGraw-Hill; 2006.
8. Spragg RP, Castro J, Li W, et al. Wetting and drying of concrete using aqueous solutions containing deicing salts. Cem Concr Compos. 2011; 33:535–542.
9. Farnam Y, Bentz D, Sakulich A, et al. Measuring freeze and thaw damage in mortars containing deicing salt using a low-temperature longitudinal guarded comparative calorimeter and acoustic emission. Adv Civ Eng Mater. 2014; 3:20130095.
10. Villani C, Farnam Y, Washington T, et al. Performance of conventional portland cement and calcium silicate based carbonated cementitious dystems furing freezing and thawing in the presence of calcium chloride deicing salts. Transp. Res. Board. 2015
11. Farnam Y, Bentz D, Hampton A, Weiss W. Acoustic emission and low-temperature calorimetry study of freeze and thaw behavior in cementitious materials exposed to sodium chloride salt. Transp Res Rec J Transp Res Board. 2014; 2441:81–90.
12. Farnam Y, Todak H, Spragg R, Weiss J. Electrical response of mortar with different degrees of saturation and deicing salt solutions during freezing and thawing. Cem Concr Compos. 2015; 59:49–59.
13. Farnam Y, Wiese A, Bentz D, et al. Damage Development in Cementitious Materials Exposed to Magnesium Chloride Deicing Salt. Constr Build Mater. 2015; 93:384–392.
14. Han B, Choi JH, Dantzig Ja, Bischof JC. A quantitative analysis on latent heat of an aqueous binary mixture. Cryobiology. 2006; 52:146–151. [PubMed: 16337621]
15. Radjy F. A thermodynamic study of the system hardened cement paste and water and its dynamic mechanical response as a function of temperature. 1968
16. Young JF. A review of the pore structure of cement paste and concrete and its influence on permeability. 1988; 108:1–18.
17. Whiting DA, Nagi MA. Manual on control of air content in concrete. 1998
18. Kumar R, Bhattacharjee B. Porosity, pore size distribution and in situ strength of concrete. Cem Concr Res. 2003; 33:155–164.
19. Castro J, Bentz D, Weiss J. Effect of sample conditioning on the water absorption of concrete. Cem Concr Compos. 2011; 33:805–813.
20. Sun Z, Scherer GW. Effect of air voids on salt scaling and internal freezing. Cem Concr Res. 2010; 40:260–270.
21. Li W, Pour-Ghaz M, Castro J, Weiss J. Water absorption and critical degree of saturation relating to freeze-thaw damage in concrete pavement joints. J Mater Civ Eng. 2012; 24:299–307.
22. Cai H, Liu X. Freeze-thaw durability of concrete: ice formation process in pores. Cem Concr Res. 1998; 28:1281–1287.
23. Li W, Sun W, Jiang J. Damage of concrete experiencing flexural fatigue load and closed freeze/thaw cycles simultaneously. Constr Build Mater. 2011; 25:2604–2610.
24. Sun Z, Scherer GW. Pore size and shape in mortar by thermoporometry. Cem Concr Res. 2010; 40:740–751.
25. Andersson K, Allard B, Bengtsson M, Magnusson B. Chemical composition of cement pore solutions. Cem Concr Res. 1989; 19:327–332.
26. Pigeon, M.; Pleau, R. Durability of concrete in cold climates. CRC Press; 2010.
27. Beddoe R, Setzer M. A low-temperature DSC investigation of hardened cement paste subjected to chloride action. Cem Concr Res. 1988; 18:249–256.
28. Askeland DR, Pradeep PP. The science and engineering of materials. Cengage Learning. 2003
29. Debenedetti P. Supercooled and glassy water. J. Phys. Condens. Matter 15.45. 2003; 1669
30. Wilding CR. The performance of cement based systems. Cem Concr Res. 1992; 22:299–310.
31. Qian, Y.; Farnam, Y.; Weiss, J. Using acoustic emission to quantify freeze–thaw Damage of mortar saturated with naCl solutions; Proc. 4th Int. Conf. Durab. Concr. Struct; 2014. p. 32-37.
32. Sun Z, Scherer GW. Measurement and simulation of dendritic growth of ice in cement paste. Cem Concr Res. 2010; 40:1393–1402.
33. Thomas, LC. Heat transfer. Englewood Cliffs, N.J.: Prentice Hall;

34. Velraj R, Seeniraj RV, Hafner B, et al. Heat transfer enhancement in a latent heat storage system. Sol Energy. 1999; 65:171–180.
35. Lecomte D, Mayer D. Design method for sizing a latent heat store/heat exchanger in a thermal system. Appl Energy. 1985; 21:55–78.
36. Costa M, Buddhi D, Oliva A. Numerical simulation of a latent heat thermal energy storage system with enhanced heat conduction. Energy Convers Manag. 1998; 39:319–330.
37. Bentz, D. A computer model to predict the surface temperature and time-of-wetness of concrete pavements and bridge decks. US Department of Commerce, Technology Administration, National Institute of Standards and Technology; 2000.
38. Bentz DP, Turpin R. Potential applications of phase change materials in concrete technology. Cem Concr Compos. 2007; 29:527–532.
39. Zivkovic B, Fujii I. An analysis of isothermal phase change of phase change material within rectangular and cylindrical containers. Sol Energy. 2001; 70:51–61.
40. Ismail KAR, Abugderah MM. Performance of a thermal storage system of the vertical tube type. Energy Convers Manag. 2000; 41:1165–1190.
41. Hamada Y, Ohtsu W, Fukai J. Thermal response in thermal energy storage material around heat transfer tubes: effect of additives on heat transfer rates. Sol Energy. 2003; 75:317–328.
42. Voller VR, Swaminathan CR. Treatment of discontinuous thermal conductivity in control-volume solutions of phase-change problems. Numer Heat Transf Part B Fundam. 1993; 24:161–180.
43. Ismail KAR, Da Silva M das GE. Numerical solution of the phase change problem around a horizontal cylinder in the presence of natural convection in the melt region. Int J Heat Mass Transf. 2003; 46:1791–1799.
44. Fukai J, Hamada Y, Morozumi Y, Miyatake O. Improvement of thermal characteristics of latent heat thermal energy storage units using carbon-fiber brushes: experiments and modeling. Int J Heat Mass Transf. 2003; 46:4513–4525.
45. Gong Z-X, Mujumdar AS. Finite-element analysis of cyclic heat transfer in a shell-and-tube latent heat energy storage exchanger. Appl Therm Eng. 1997; 17:583–591.
46. Rubinsky B, Cravahlo EG. A finite element method for the solution of one-dimensional phase change problems. Int J Heat Mass Transf. 1981; 24:1987–1989.
47. Yoo J, Rubinsky B. Numercial computation using finite elements for the moving interface in heat transfer problems with phase transformation. Numer Heat Transf. 2007; 6:209–222.
48. Shamsundar N, Sparrow EM. Analysis of multidimensional conduction phase change via the enthalpy model. J Heat Transfer. 1975; 97:333.
49. Hibbert SE, Markatos NC, Voller VR. Computer simulation of moving-interface, convective, phase-change processes. Int J Heat Mass Transf. 1988; 31:1785–1795.
50. Smith, WF.; Hashemi, J. Foundations of materials science and engineering. 4th. McGraw-Hill; 2006.
51. Callister WD, Rethwisch D. Materials science and engineering: An introduction. 2009
52. West Conhoshocken, PA: ASTM International; ASTM E1225-09. Standard Test Method for Thermal Conductivity of Solids by Means of the Guarded-Comparative-Longitudinal Heat Flow Technique.
53. ASTM D5470-12: Standard Test Method for Thermal Transmission Properties of Thermally Conductive Electrical Insulation Materials 1.
54. Incropera, FP.; DeWitt, DP.; Bergman, TL.; Lavine, AS. Fundamentals of heat and mass transfer. John Wiley & Sons; 2007.
55. Litvan G. Phase transitions of adsorbates: IV, mechanism of frost action in hardened cement paste. J Am Ceram Soc. 1972; 55:38–42.
56. Brun M, Lallemand A, Quinson J-F, Eyraud C. A new method for the simultaneous determination of the size and shape of pores: the thermoporometry. Thermochim Acta. 1977; 21:59–88.
57. Radlinska A, Rajabipour F, Bucher B, et al. Shrinkage mitigation strategies in cementitious systems: A closer look at differences in sealed and unsealed behavior. Transp Res Rec J Transp Res Board. 2008; 2070:59–67.

58. Henkensiefken R, Bentz D, Nantung T, Weiss J. Volume change and cracking in internally cured mixtures made with saturated lightweight aggregate under sealed and unsealed conditions. Cem Concr Compos. 2009; 31:427–437.
59. Yang Z, Weiss WJ, Olek J. Water transport in concrete famaged by tensile loading and freeze–thaw cycling. J Mater Civ Eng. 2006; 18:424–434.
60. Sourirajan S, Kennedy GC. The system H2O-NaCl at elevated temperatures and pressures. Am J Sci. 1962; 260:115–141.
61. Levy O, Stroud D. Maxwell Garnett theory for mixtures of anisotropic inclusions: Application to conducting polymers. Phys Rev B. 1997; 56:8035–8046.
62. Progelhof RC, Throne JL, Ruetsch RR. Methods for predicting the thermal conductivity of composite systems: A review. Polym Eng Sci. 1976; 16:615–625.
63. Touloukian, et al. Thermophysical properties of matter. 1970
64. Hilsenrath, et al. Tables of thermal properties of gases. NBS Circ. 1955:564.
65. Fletcher, NH. The Chemical Physics of Ice. Cambridge Univ. Press; 2009.
66. Pitzer KS, Peiper JC, Busey RH. Thermodynamic properties of aqueous sodium chloride solutions. J. Phys. Chem. 1984 Ref. Data 13.
67. Campbell-Allen D, Thorne CP. The thermal conductivity of concrete. Mag Concr Res. 1963; 15:39–48.
68. Daian J-F. Condensation and isothermal water transfer in cement mortar Part I — Pore size distribution, equilibrium water condensation and imbibition. Transp Porous Media. 1988; 3:563–589.
69. Bentz D, Peltz M, Duran-Herrera A, et al. Thermal properties of high-volume fly ash mortars and concretes. J Build Phys. 2010; 34:263–275.
70. Zhou L-P, Wang B-X, Peng X-F, et al. On the Specific Heat Capacity of CuO Nanofluid. Adv Mech Eng. 2010; 2010:1–4.
71. Farnam, Y.; Esmaeeli, HS.; Bentz, D., et al. Experimental and Numerical Investigation on the Effect of Cooling/Heating Rate on the Freeze-Thaw Behavior of Mortar Containing Deicing Salt Solution; Int. Conf. Regen. Conserv. Concr. Struct; 2015.
72. Farnam Y, Krafcik M, Liston L, et al. Evaluating the Use of Phase Change Materials in Concrete Pavement to Melt Ice and Snow. J Mater Civ Eng. 2015; 04015161
73. Williams RJJ, Aldao CM. Thermal conductivity of plastic foams. Polym Eng Sci. 1983; 23:293–298.

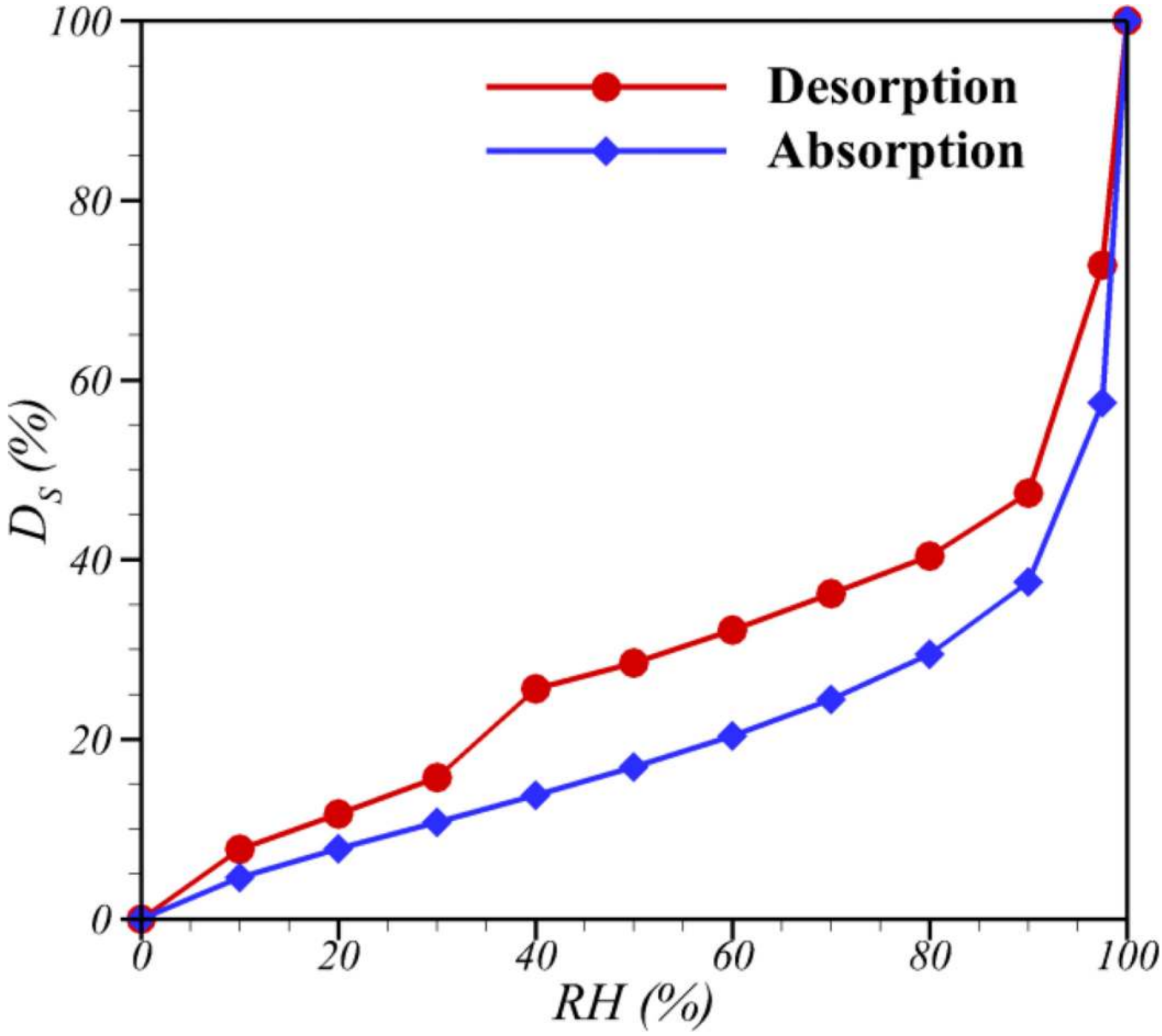

Figure 1.
Desorption-absorption isotherms of mortar specimen.

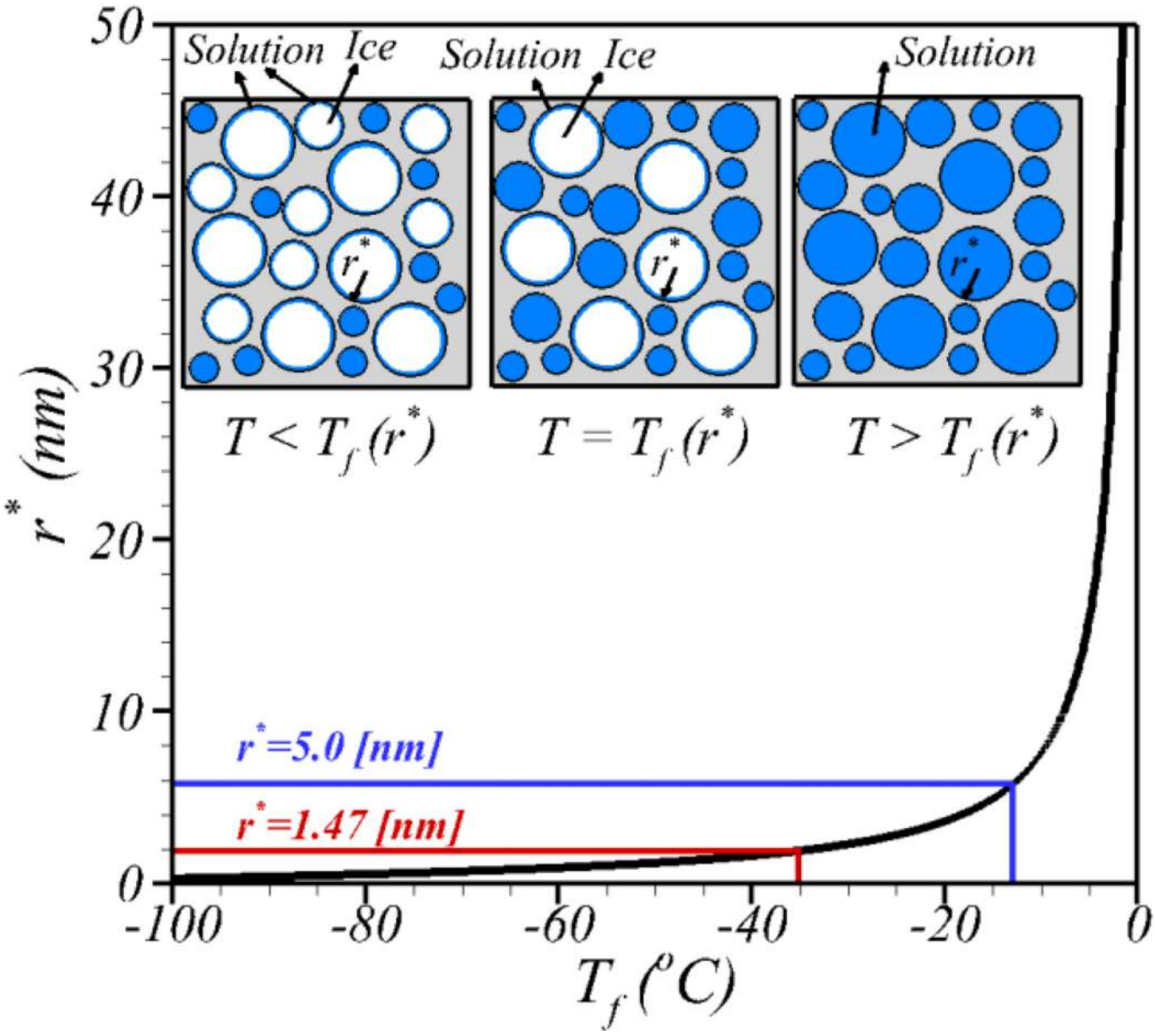

Figure 2.

The effect of pore size on the freezing temperature of water using the Gibbs-Thomson equation, including a schematic of ice formation in a porous material (inset).

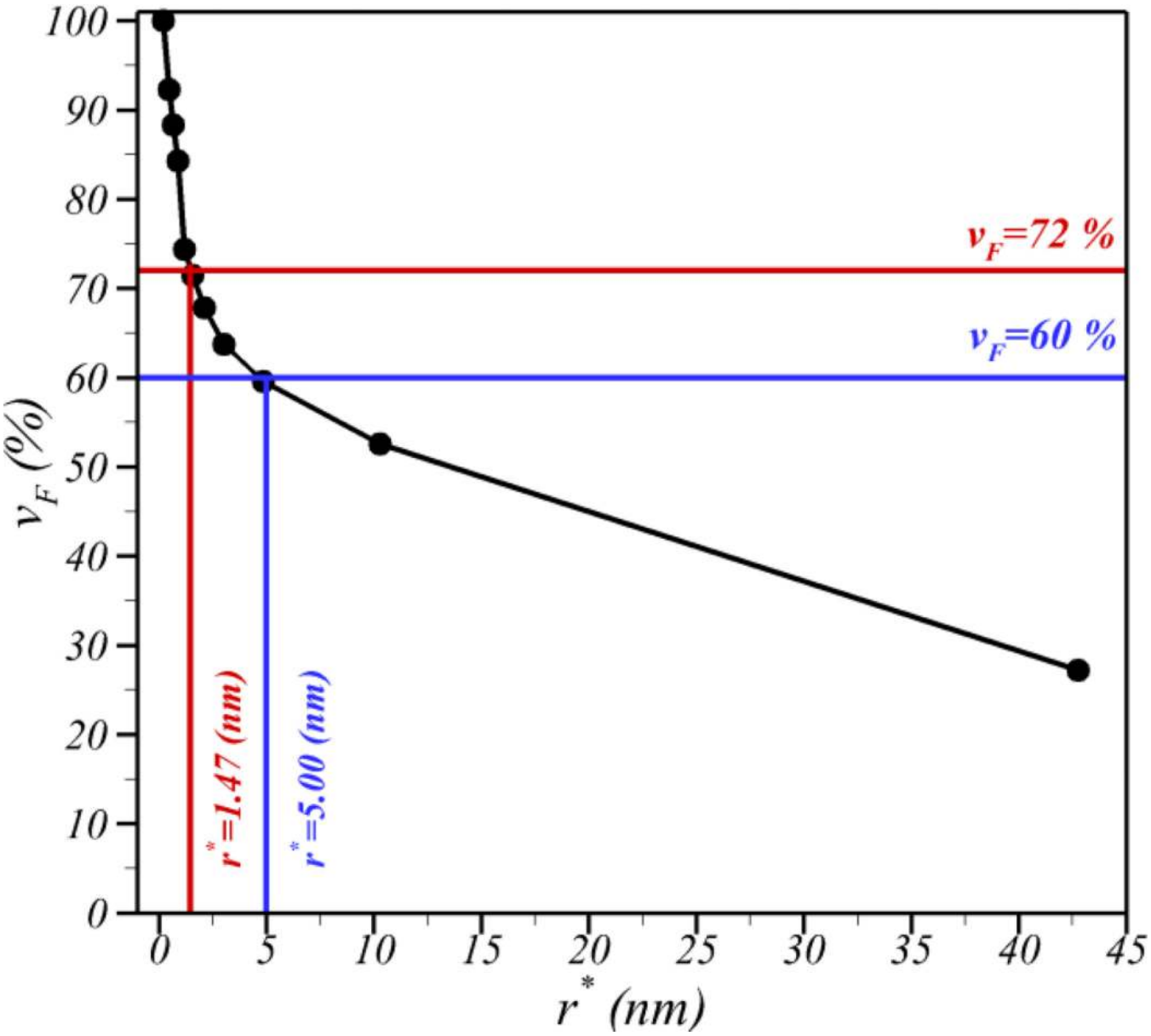

Figure 3.
Volume fraction of pore solution that can freeze as a function of the critical nucleus (pore) size.

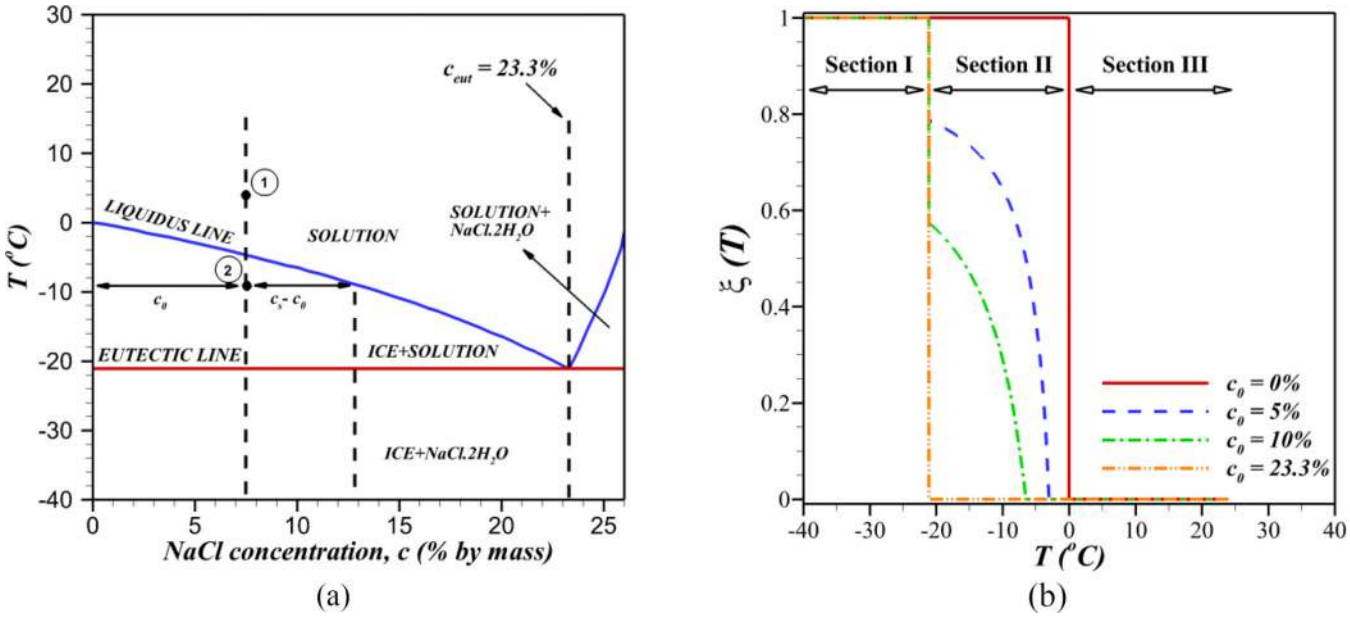

Figure 4.

(a) Phase diagram for aqueous NaCl solution [60]; (b) the fraction of produced ice as a function of temperature within the freezing region for bulk NaCl solution.

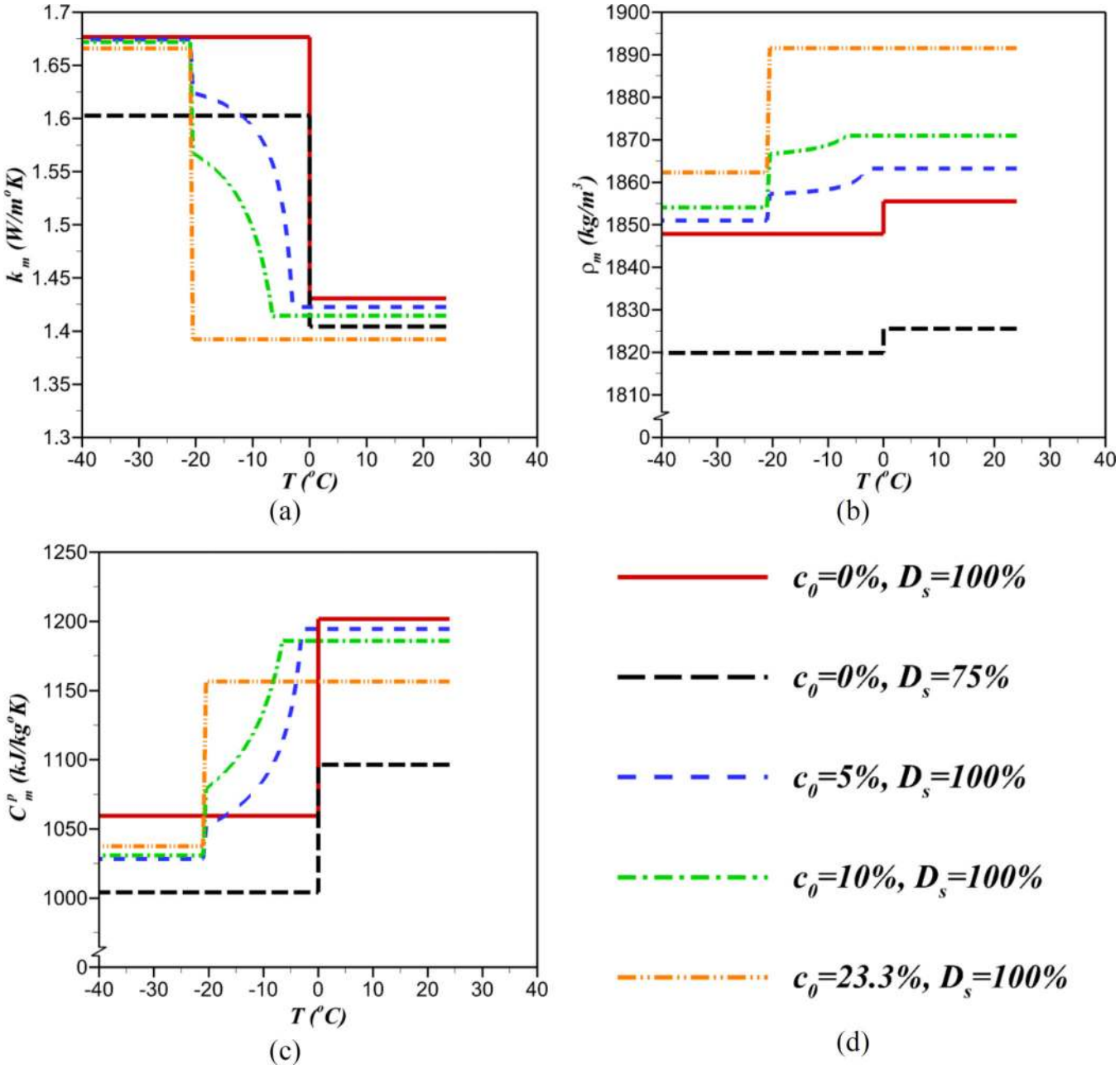

Figure 5.

Calculated effective (a) thermal conductivity (k_m); (b) density (ρ_m); and (c) specific heat capacity (C_m^p) as a function of temperature for mortar specimens containing (d) various concentrations of NaCl solutions and different degrees of saturation.

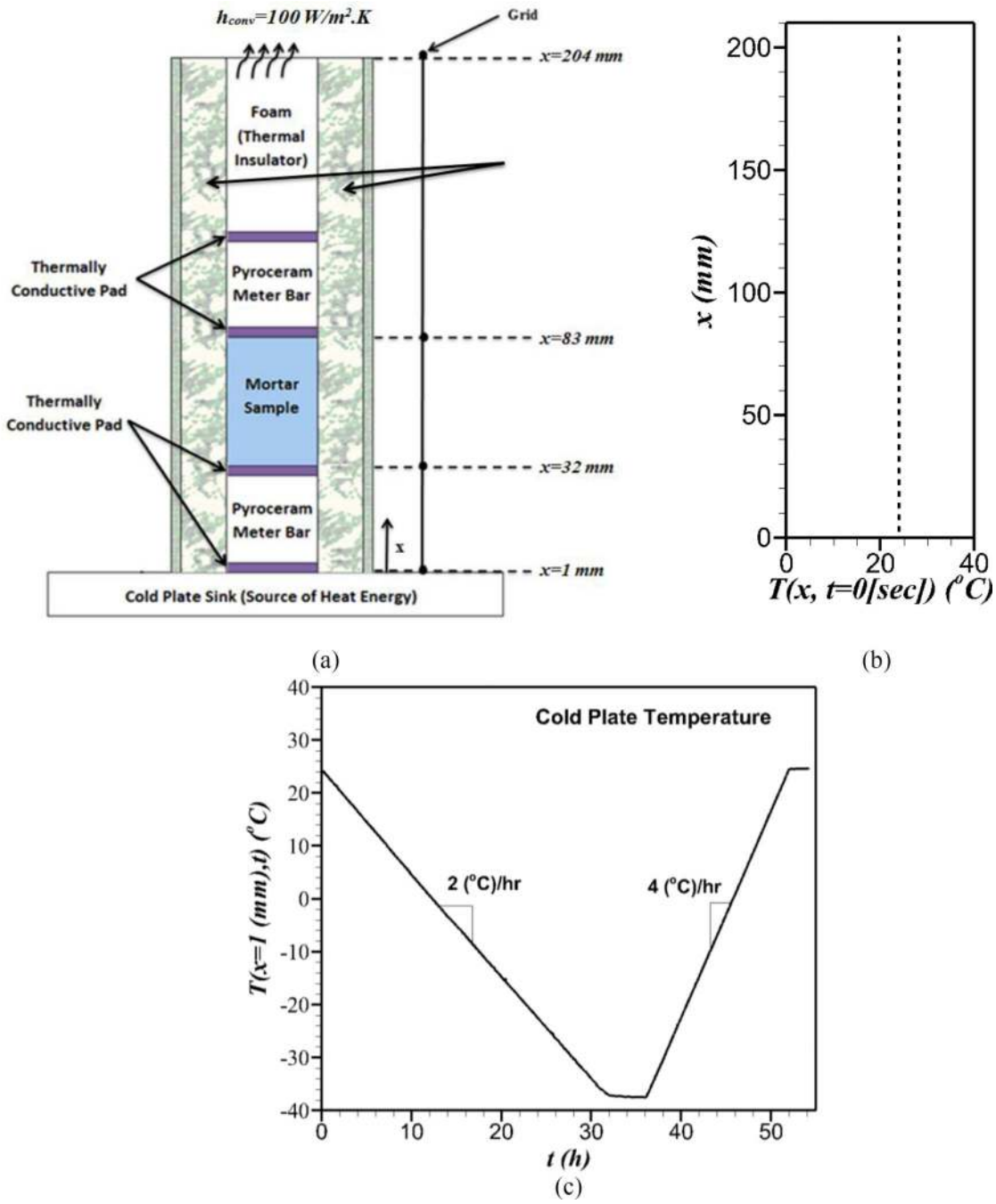

Figure 6.

(a) Schematic view of LGCC experiment with adapted finite difference nodes; (b) initial temperature of finite difference simulation, i.e., T (x,t = 0); and (c) temperature at the bottom of the LGCC experiment, i.e., T (x = 1,t), as a function of time.

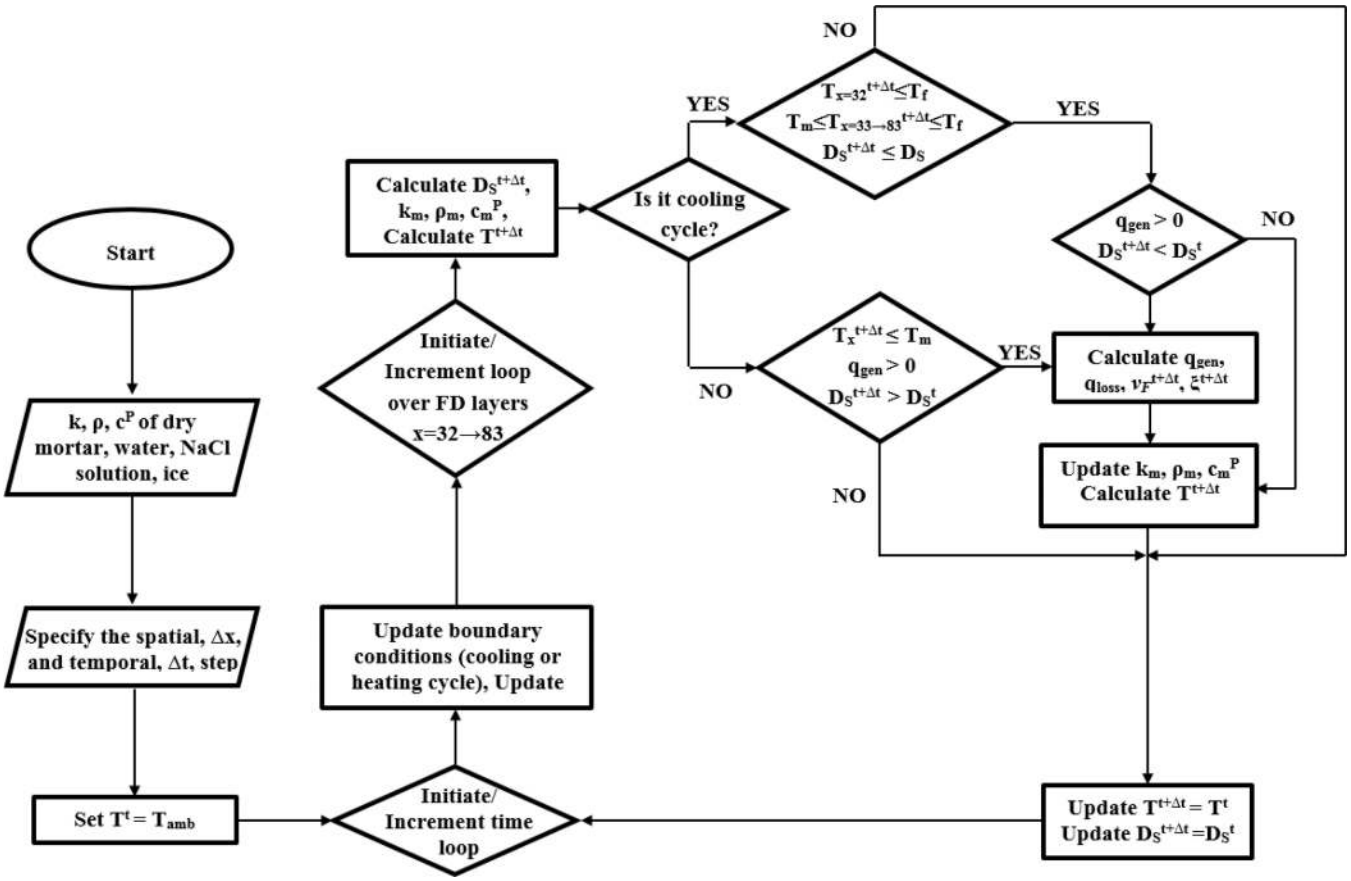

Figure 7.

Numerical algorithm of finite difference strategy using heat transfer equation to simulate the thermal behavior of a saturated mortar specimen.

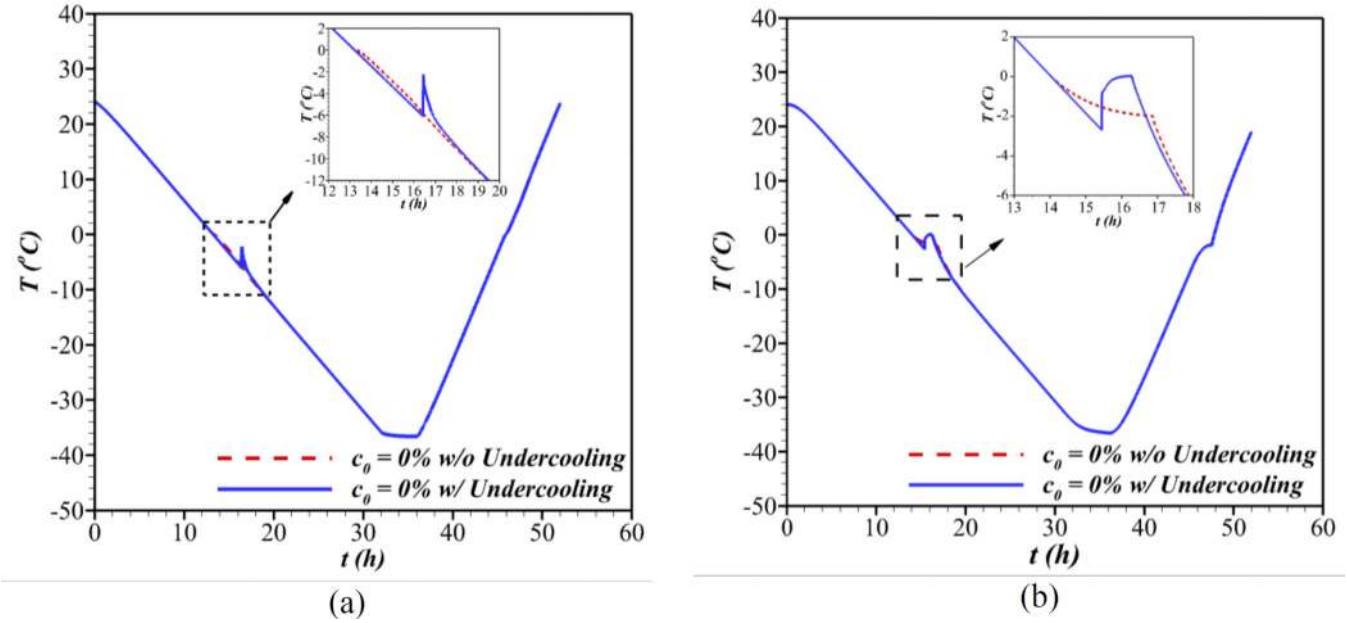

Figure 8.

The effect of including undercooling in the numerical simulation on temperature profile of saturated mortar specimen containing water (0 % NaCl) exposed to one freeze-thaw cycle at different locations of mortar specimen: (a) x = 32 mm; (b) at x = 83 mm (see Figure 1 for definition).

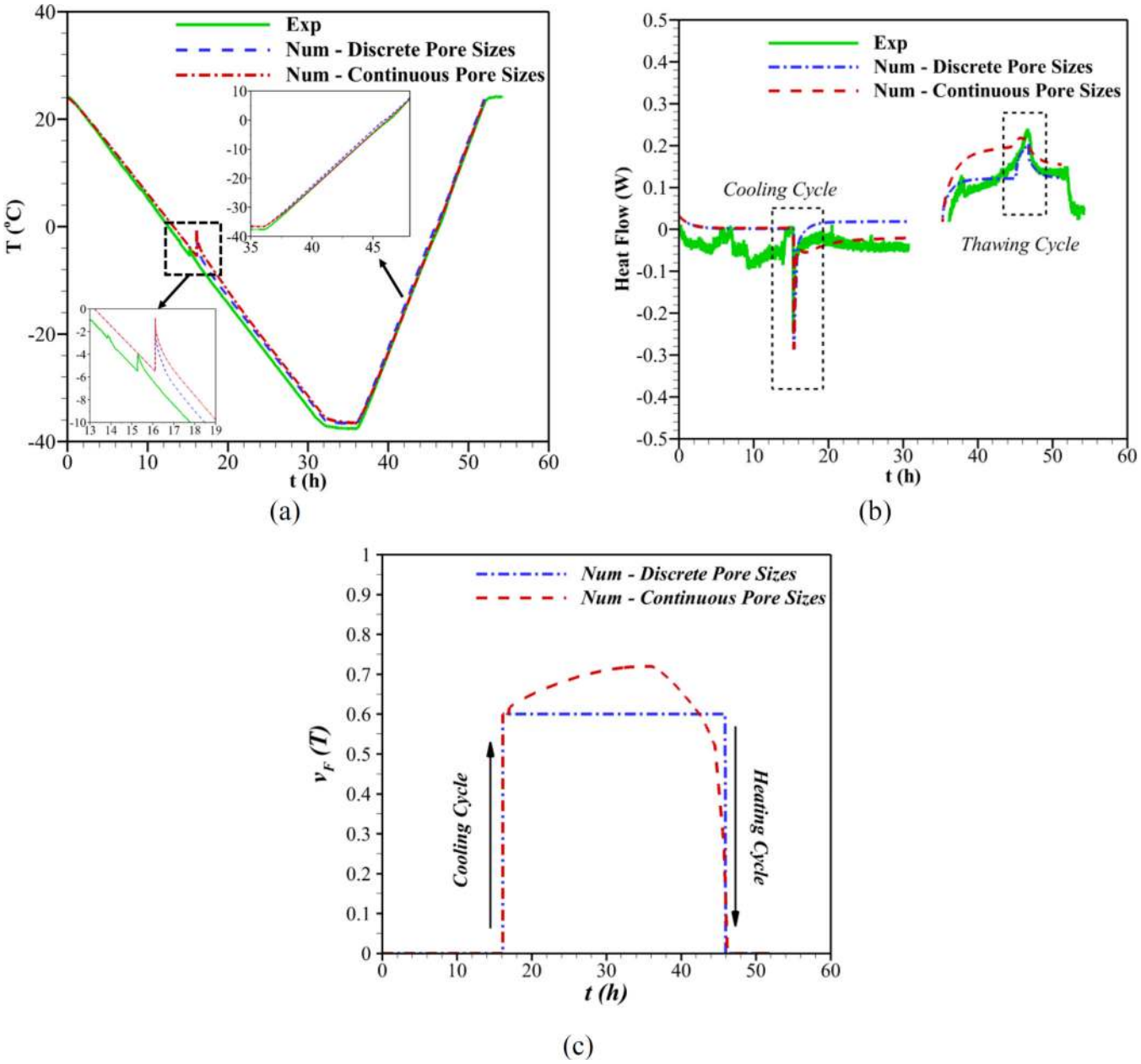

Figure 9.

Experimental and numerical results for mortar specimen fully saturated with water (a) temperature profiles at $x = 32$ mm (see Figure 1 for definition of x); (b) predicted heat flow; (c) volume of pore solution undergoes phase transformation at the bottom surface of the mortar specimen.

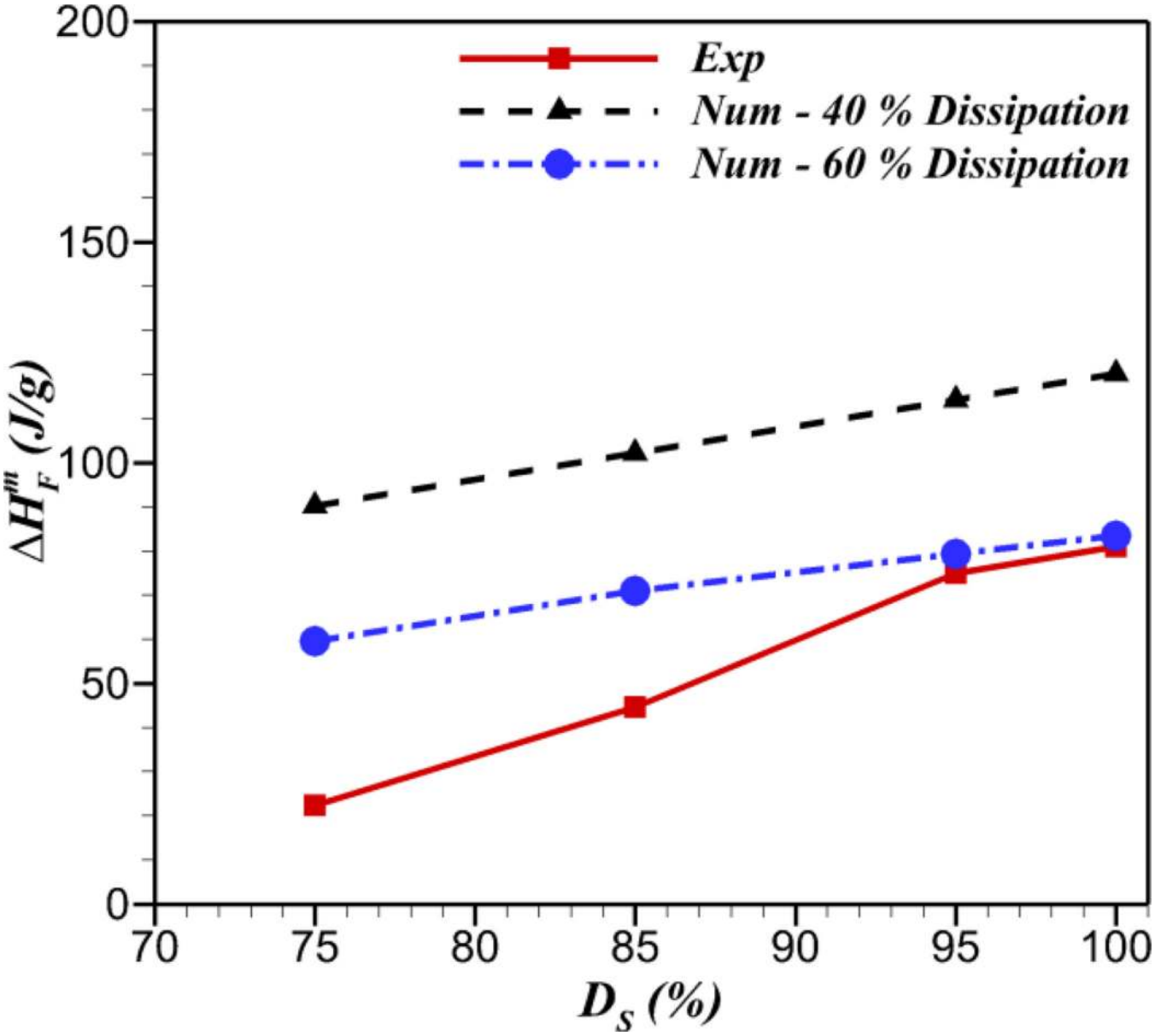

Figure 10.

The amount of heat release during freezing $\left(\Delta H_m^F\right)$ for the mortar specimen saturated at different degrees of saturations (D_S).

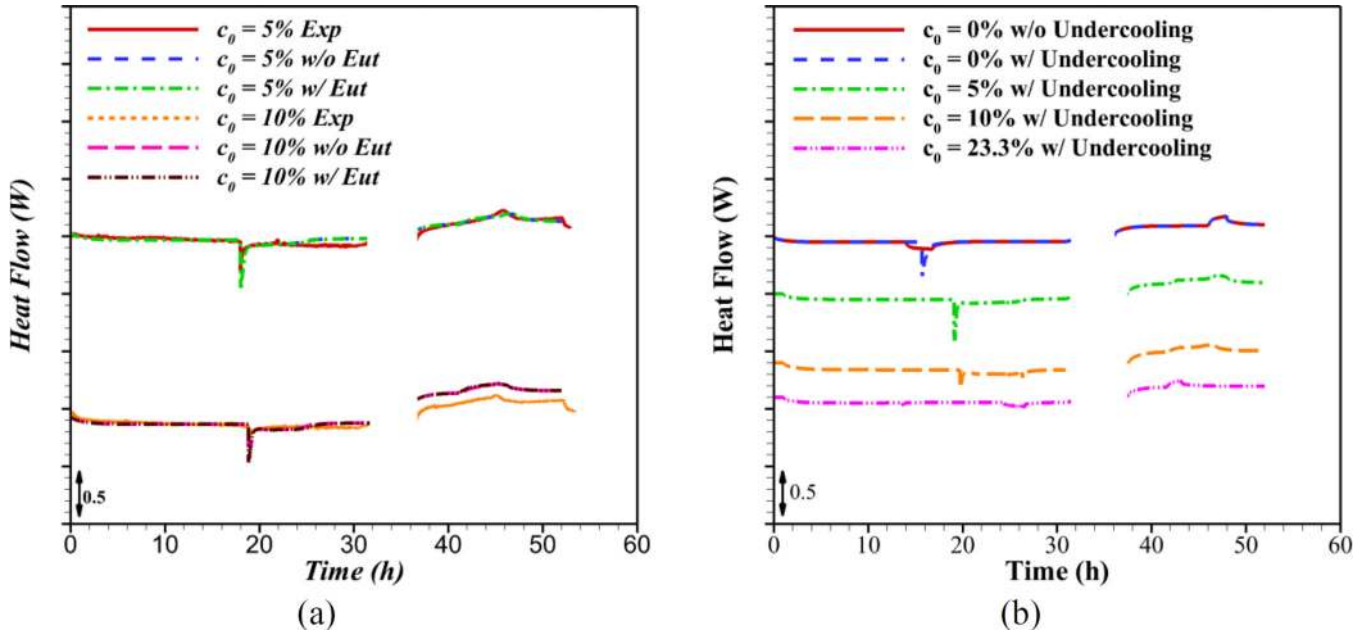

Figure 11.

Heat flow as a function of time for mortar specimens saturated with NaCl solution obtained from (a) experimental results and numerical simulation to investigate the role of eutectic phase transformation; (b) numerical simulations at various concentrations (0 %, 5 %, 10 %, 23.3 %).

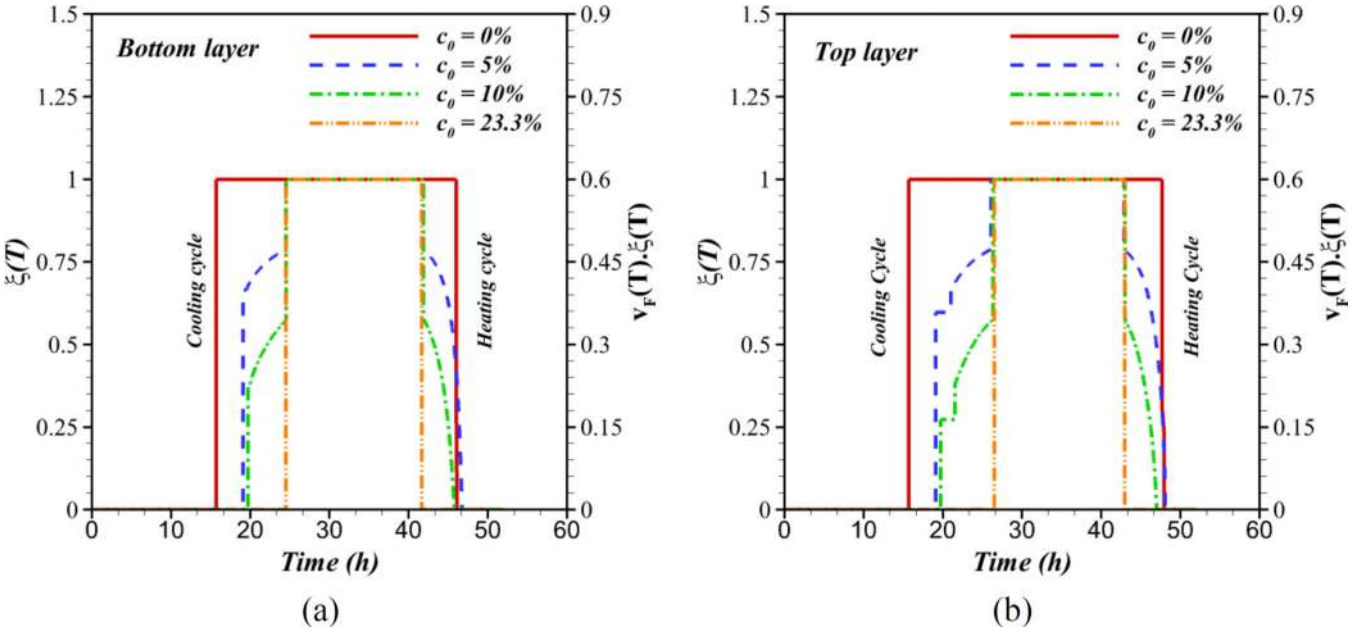

Figure 12.

Frozen fraction of pore solution of the mortar specimen saturated using NaCl solution as a function of time at (a) the bottom layer (x = 32 mm); and (b) the top layer (x = 83 mm).

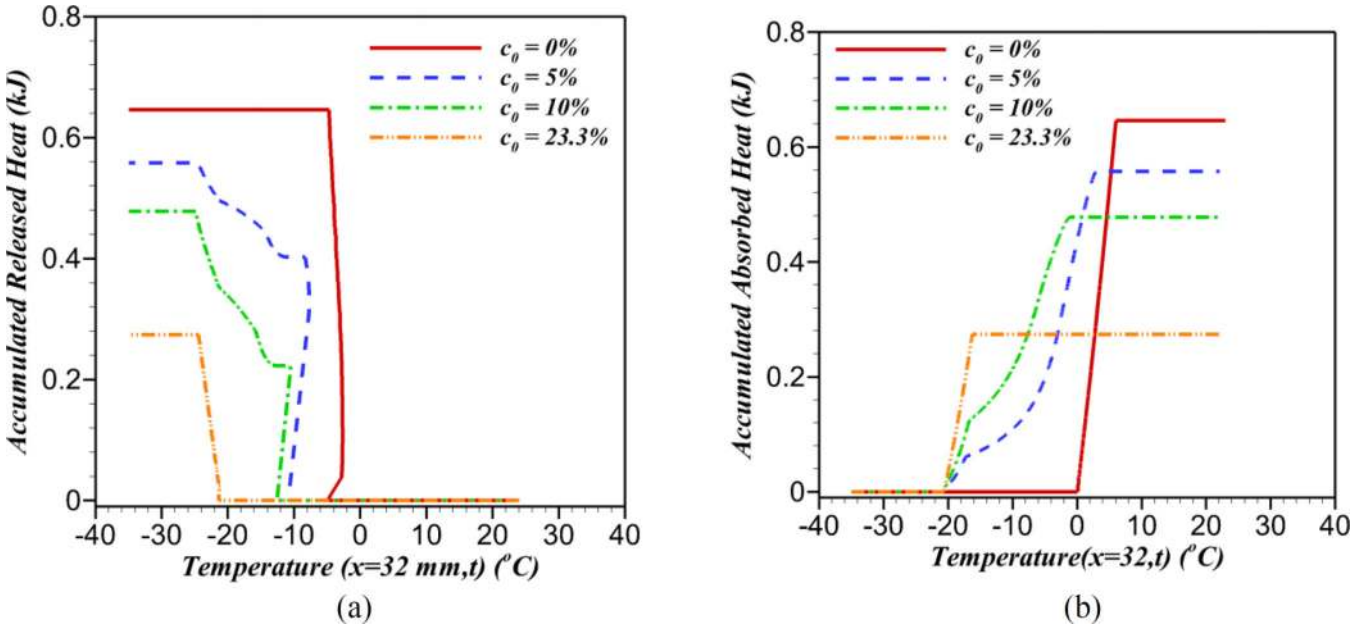

Figure 13.

Accumulated heat as a function of temperature for mortar specimen with 5 %, 10 %, and 23.3 % NaCl concentration (a) heat released by the specimen during one freezing cycle; (b) heat absorbed by the specimen during one thawing cycle versus cold plate temperature.

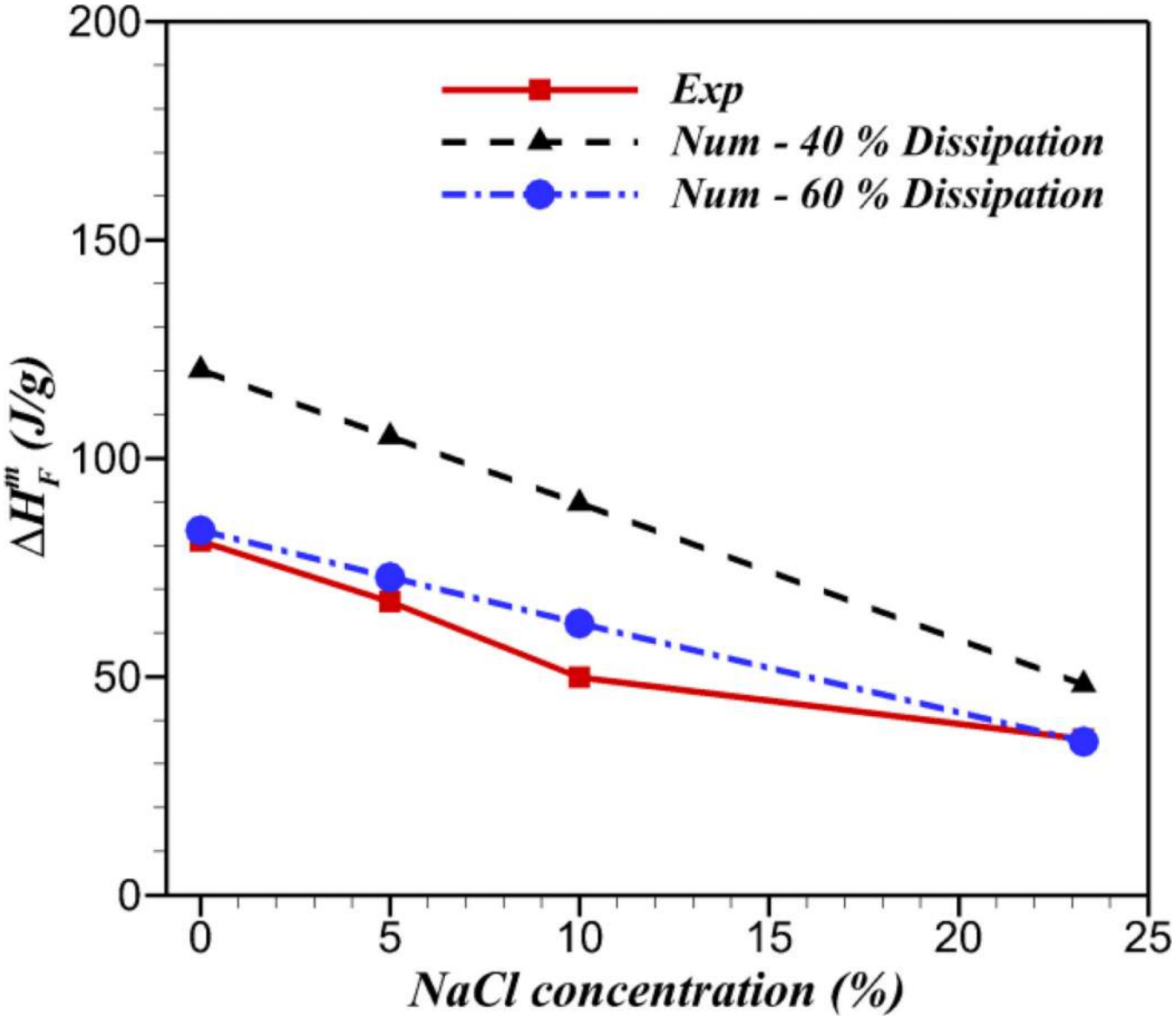

Figure 14.

The amount of heat release during freezing $\left(\Delta H_m^F\right)$ for the mortar specimen saturated with different NaCl solutions.

Table 1

Thermal properties of air, ice and NaCl solution with different concentrations

Material	k (W/(m·K))	ρ (kg/m^3)	C^p (kJ/(kg·K))
Air [63, 64]	0.023	1.35	1.005
Ice [65]	2.25	934	2030
0% NaCl solution [66]	0.5886	997	4121
5% NaCl solution [66]	0.5611	1036	3947
10% NaCl solution [66]	0.5336	1074	3773
23.3% NaCl solution [66]	0.46	1178	3310
Dry mortar [67–69]	1.7	2070	850

Table 2

Thermal properties of thermally conductive pad, foam and Pyroceram code 9606

Material	***k* (*W*/(*m*·*K*))**	**ρ (*kg*/*m*^{3})**	***C*^{p} (*kJ*/(*kg*·*K*))**
Thermal Pad	3.0	309	850
Foam [73]	0.03	20	1340
Pyroceram Code 9606 [9]	*	2600	900

Note:

* The thermal conductivity of Pyroceram code 9606 as a meter bar material was calculated as a function of temperature [9].

Table 3

Freezing and melting points of saturated mortar specimens with NaCl solutions [11]

NaCl Solution Concentration (%)	Freezing Point T_f (°C)	Melting Point T_m (°C)	Amount of Undercooling with Respect to Liquidus Line**
0	−6.1	0.0	−6.1
5	−10.8	−3.0	−7.8
10	−12.0	−6.5	−5.5
23.3*	−21.1	−21.1	0

Note:

* For specimens containing 23.3% NaCl solution, the freezing point and melting point are identical (T_{eut}) since these points are located at the eutectic line and the entire solution only forms eutectic solid during solidification.

** The amount of undercooling is calculated by subtracting the melting point T_m from the freezing point T_f of the corresponding bulk NaCl solution.